Mon. Not. R. Astron. Soc. **000**, 000–000 (0000) Printed 10 June 2016 (MN LATEX style file v2.2)

Very Large Telescope Deep Echelle Spectroscopy of Galactic Planetary Nebulae NGC 6153, M 1-42 and Hf 2-2⋆

I. A. McNabb[1], X. Fang[2,3,4]†, and X.-W. Liu[1,5]
[1]*Kavli Institute for Astronomy and Astrophysics, Peking University, Beijing 100871, China*
[2]*Instituto de Astrofísica de Andalucía - CSIC, Glorieta de la Astronomía, s/n. E-18008 Granada, Spain*
[3]*Laboratory for Space Research, Faculty of Science, University of Hong Kong, Pokfulam Road, Hong Kong, China*
[4]*Department of Physics, University of Hong Kong, Pokfulam Road, Hong Kong, China*
[5]*Department of Astronomy, School of Physics, Peking University, Beijing 100871, China*

arXiv:1606.02925v1 [astro-ph.SR] 9 Jun 2016

Received XXXX, accepted XXXX, Published online XXX

ABSTRACT

We present deep spectroscopy of three Galactic planetary nebulae (PNe) with large abundance discrepancy factors (ADFs): NGC 6153, M 1-42 and Hf 2-2. The spectra were obtained with VLT/UVES and cover the whole optical range (3040–11 000 Å) with a spectral resolution of ∼20 000. For all three PNe, several hundred emission lines were detected and identified, with more than 70 per cent of them as permitted lines. Most of these permitted lines are excited by recombination. Numerous weak optical recombination lines (ORLs) of O II, C II, N II and Ne II were detected in the spectra and accurate fluxes measured. Line flux tables were compiled and ready for use by the community of nebular astrophysics. These ORLs were critically analyzed using the effective recombination coefficients recently calculated for the optical recombination spectrum of N II and O II under the physical conditions of photoionized gaseous nebulae. Plasma diagnostics based on the heavy element ORLs were carried out using the new atomic data. Elemental abundances derived from the ORLs were systematically higher than those derived from the collisionally excited lines (CELs) by a factor of ∼11, 22 and 80 for NGC 6153, M 1-42 and Hf 2-2, respectively. The electron temperatures derived from the heavy element ORLs are systematically lower than those derived from the CELs. These ORL versus CEL abundance and temperature discrepancies, previously observed in the three PNe through deep spectroscopy with medium to low spectral resolution, are thus confirmed by our analysis of the deep echelle spectra using the new atomic data.

Key words: line: identification – atomic data – atomic processes – ISM: abundances – planetary nebulae: individual: NGC 6153, M 1-42, Hf 2-2

1 INTRODUCTION

Planetary nebulae (PNe) evolve from the low- and intermediate-mass (⩽8–10 $M_{\odot}$) stars, and are common in the universe. They are characterized by rich, bright mission line spectrum that act as a vital tool to acquire knowledge of their chemical composition. This chemical information sheds lights on the basic astrophysics regarding the formation and evolution of the progenitor stars. Since the α-elements are in principle not enriched through nucleosynthesis inside the low- and intermediate-mass stars, the abundances of O, Ne, S, Ar and Cl of a PN represent the chemistry of the interstellar medium (ISM) at the time when its progenitor star formed. The bright and narrow emission lines of PNe make them not only observable at very distant (∼100 Mpc; Gerhard et al. 2005, 2007) galaxies but also excellent tracers of kinematics (e.g., Longobardi et al. 2015a,b).

The traditional method for the analysis of PN spectra and deriving ionic abundances is mainly based on the strong collisionally excited lines (CELs; also usually called the forbidden lines) of heavy elements. However, emissivities of the CELs relative to that of Hβ are very sensitive to the electron temperature under typical physical conditions of the photoionized gaseous nebulae, and therefore the derived ionic abundances could be greatly underestimated if temperature fluctuations exist. These electron temperatures are derived using the traditional method based on the CEL ratios (Osterbrock & Ferland 2006). Another method of nebular analysis utilizes the intensity ratio of an optical recombination line (ORL) of either helium or a heavy element with the Hβ (see the reviews Liu 2003, 2006a,b). Unlike the CELs, the relative emissivities of ORLs change weakly with both temperature and density because they only have a power-law dependence on the temperature and negligible dependence on the density (e.g., Liu 2006a,b). This

⋆ Based on observations collected at the European Southern Observatory, Chile. Proposal ID ESO 69.D-0174(A).

† E-mail: fangx@hku.hk

method is thus much less affected by temperature fluctuations, and the abundances derived from ORLs are expected to be more reliable. However, accurate measurements of the heavy element ORLs are extremely demanding due to their weakness ($\sim10^{-4}$–10^{-3} of the Hβ flux, or even fainter), while the typical fluxes of the CELs are more than 10^3–10^4 times those of the heavy element ORLs (e.g., the [O III] λ5007 line is usually 10 times the Hβ flux).

Modern technologies in observations have enabled detection of many heavy element ORLs that were previously too weak to be detected. The recombination lines of O II, C II, N II, and Ne II, can now be measured with high accuracy in the deep spectra of PNe. Some of these recombination lines are important nebular diagnostics, such as the density-sensitive ORL ratios O II λ4649/λ4662 and N II λ5679/λ5666 and the temperature-sensitive ratios O II λ4649/λ4089 and N II λ5679/λ4041, which have recently been applied to nebular analysis (e.g., McNabb et al. 2013; Fang & Liu 2013). Accompanied with the steady improvement of observational technologies, atomic data calculations, especially for the effective recombination coefficients for nebular lines of the heavy element ions, have achieved significant progress over the past decades. Calculations of the accurate atomic data can help the astrophysical community to better understand the physics in gaseous nebulae as well as the excitation mechanisms of emission, and this effort is no doubt an organic part of nebular astrophysics (Ferland 2003). Plasma diagnostics of Galactic PNe and H II regions based on the heavy element ORLs have been carried out with the availability of new atomic data (e.g., McNabb et al. 2013). Among the calculations for the relatively abundant heavy elements in the nebulae, the most comprehensive treatment of the recombination and radiative-collisional processes has been for the nebular lines of N II (Fang, Storey & Liu 2011, 2013) and O II (P. J. Storey, unpublished; private communications). These new effective recombination coefficients enabled plasma diagnostics using the ORLs of heavy elements (McNabb et al. 2013).

Nebular analyses based on the CELs and ORLs/continua have revealed one of the key problems in nebular astrophysics: the ionic and elemental abundances of carbon, nitrogen, oxygen and neon relative to hydrogen derived from ORLs are systematically higher than those derived from the much brighter CELs. This phenomenon, known as the "abundance discrepancy", was originally noticed in the *IUE* observations of the C^{2+}/H^+ abundance ratio derived from the C III] $\lambda\lambda$1907, 1909 forbidden/semi-forbidden lines and the ground-based spectroscopic observations of the same ionic abundance derived from the C II λ4267 line (e.g., Barker 1982, 1991, and references therein). Another discrepancy in nebular studies that has been proved to be related with the "abundance discrepancy" is that the nebular electron temperature derived from the Balmer jump (at 3646 Å) is always lower than those derived from the CEL ratios (e.g., Peimbert 1971; Liu & Danziger 1993).

The "abundance discrepancy" problem has been investigated in some particular Galactic PNe: e.g., NGC 7009 (Liu et al. 1995; Luo, Liu & Barlow 2001), NGC 6153 (Liu et al. 2000), M 1-42 and M 2-36 (Liu et al. 2001), NGC 6543 (Wesson & Liu 2004), Hf 2-2 (Liu et al. 2006), and NGC 6720 (Garnett & Dinerstein 2001). Spectroscopic surveys of Galactic PNe (e.g., Tsamis et al. 2003, 2004; Liu et al. 2004a,b; Robertson-Tessi & Garnett 2005; Wesson, Liu & Barlow 2005; Wang & Liu 2007) have also been carried out, which allows investigation of the distribution of the abundance discrepancy among the PNe (Liu 2012a). The abundance discrepancy factor (ADF), defined as the ratio of the ORL and CEL abundances of the same ion, lies in the range 1.6–3.2 for most Galactic PNe (Liu 2006b). There are many PNe with ADFs $\sim$5–20. The highest ADF has been discovered in Hf 2-2 (ADF$\sim$70; Liu et al. 2006). Different from PNe, where the ADF values span a wide range, ADFs of H II regions are mostly between 1 and 2 (e.g., García-Rojas & Esteban 2007).

Over decades of research in PNe and H II regions, several mechanisms have been suggested to explain the abundance and temperature discrepancies (e.g., Peimbert 1967; Rubin 1989; Viegas & Clegg 1994; Liu et al. 2000; see also reviews by Liu 2006a,b and Peimbert & Peimbert 2006). The discrepancies have been traditionally interpreted in terms of large temperature fluctuations by Peimbert (1967), who first revealed the temperature discrepancy through spectroscopic observations of H II regions. The temperature fluctuation model well explains the observed discrepancies in H II regions, but has difficulties in the interpretation of high ADFs ($>$5) in PNe, which needs such large temperature fluctuations that are difficult to explain physically. The bi-abundance nebular model (Liu et al. 2000) suggests that PNe (probably also in H II regions) contain a previously unknown, metal-rich component. This model well explains the problem. In this model, the faint optical recombination lines of heavy elements are mainly emitted from the 'cold' ($\leqslant$1000 K), metal-rich (probably H-deficient) component, where the cooling through the infrared fine-structure lines of the heavy elements is very efficient, while the stronger CELs come predominantly from the hot ($\sim10^4$ K) ionized gas with nearly Solar chemical composition. Deep recombination line surveys and spectroscopic analyses of Galactic PNe have provided strong evidence for the existence of the 'cold', metal-rich component (see the review Liu 2012a), although the origin of this component is still unclear.

Abundance calculations and temperature determinations for PNe so far have all been based on the theory that free electrons have Maxwell-Boltzmann energy distributions (Spitzer 1948), a widely accepted assumption in nebular astrophysics. Recently, Nicholls, Dopita & Sutherland (2012) proposed that energies of the free electrons in gaseous nebulae could deviate from the classical Maxwell-Boltzmann distribution and suggested that the "κ-distribution" of electron energy that has long been observed in the solar system plasmas, can explain the temperature and abundance discrepancies. The effects of this mechanism on the nebular abundance and temperature determinations have been under investigation (e.g., Dopita et al. 2013; Nicholls et al. 2012). Direct measurements of the electron energy distribution from observations is important to assess whether the Maxwell-Boltzmann distribution or the κ-distribution is more suitable for the free electrons in PNe. This purpose has been attempted by Storey & Sochi (2013), who studied the C II dielectronic recombination lines in several PNe. However, the uncertainties are too large to make any conclusion. Through studies of the H I free-bound emission near the Balmer jump of four PNe with the highest ADFs, Zhang, Liu & Zhang (2014) found that a nebular model with two Maxwell-Boltzmann components, along with the κ-distributed electron energies, can equally fit the observed H I recombination continuum. A Model fitting of the nebular continuum of Hf 2-2 (ADF$\sim$70) near the Balmer jump also favors the two components with Maxwell-Boltzmann distribution of electron energies over the κ-distributed electron energies (Storey & Sochi 2014). Atomic data calculations incorporating the κ-distributed electron energies have also been carried out for the H I recombination lines (Storey & Sochi 2015a) and the [O III] collisionally excited lines (Storey & Sochi 2015b).

Galactic PNe NGC 6153, M 1-42 and Hf 2-2 are among those with the highest ADFs. The heavy-element ORLs observed in the three objects have previously been analyzed using deep spectra with medium spectral resolution (Liu et al. 2000, 2001, 2006).

These spectra were mostly obtained at the ESO 1.52 m telescope. The deep spectroscopy revealed that ADF$\sim$10, 20 and 70 for NGC 6153, M 1-42 and Hf 2-2, respectively. The effective recombination coefficients of the heavy elements (C II, N II, O II and Ne II) used in these analyses are relatively outdated, although the results are still of high confidence. In this paper, we present deep echelle spectra of NGC 6153, M 1-42 and Hf 2-2 obtained at the ESO 8.2 m Very Large Telescope. The Ultraviolet and Visual Echelle Spectrograph used in the observations provide both broad wavelength coverage ($\sim$3040–11 000 Å) and high spectral resolution (R $\sim$20 000). These high-quality spectra will enable accurate flux measurements for the faint heavy element ORLs that are critical for nebular plasma diagnostics. With the availability of new effective recombination coefficients for the N II and O II recombination lines, it is worthwhile to reappraise the properties of the three archetypal PNe and investigate the ORL versus CEL abundance discrepancy in details.

The contents of this paper are as follows: Observations and data reduction are described in Section 2. The reduced 1D spectra are presented in Section 3. Emission line table and line identifications are presented in Section 4. We carry out plasma diagnostics in Section 5, and present the abundance analysis in Section 6. We discuss the results in Section 7, and summarize conclusions in Section 8.

2 OBSERVATIONS AND DATA REDUCTION

The spectra were obtained on June 8, 2002, using the ESO Ultraviolet and Visual Echelle Spectrograph (UVES; D'Odorico et al. 2000) on the UT2 Kueyen Telescope of the 8.2 m Very Large Telescope (VLT) at Cerro Paranal, Chile (prop. ID: 69.D-0174(A), P.I.: J. Danziger). UVES is a high-efficiency echelle spectrograph that covers a broad wavelength range, from the atmospheric cut-off at 3000 Å to about 11 000 Å. The light beam entering the telescope is split into two arms (from the UV to Blue, and Visual to Red) with a resolving power of about 40 000 when a 1 arcsec slit is used[1] (Decker et al. 2000). The dichroics DIC1 and DIC2 were used. Cross dispersers CD#1 and CD#2 were adopted for DIC1. Combined with the slit viewers, these two cross dispersers covered the wavelength ranges 303–388 nm in the blue arm and 476–684 nm in the red. For DIC2, cross dispersers CD#3 and CD#4 were used, covering the wavelength ranges 373–499 nm in the blue arm and 660–1060 nm in the red. A slit length of 10 arcsec was used in the blue arm and 13 arcsec for the red. The observations and instrument setups are summarized in Table 2.

Multiple exposures, typically long and short ones, were utilized for observations with each instrument setup. A 2 arcsec wide slit was used for the observations of NGC 6153. The long exposure is 20 min and the short exposure is 2 min. The slit has a position angle of 118° and covers the central part of the PN. Fig. 1 (panel a) shows the slit view for NGC 6153. For M 1-42, there are three exposures: a 30 min exposure with a slit width of 2 arcsec, a 15 min exposure with a slit width of 10 arcsec, and a 1 min exposure with a slit width of 2 arcsec. The slit has a position angle of 120° covering the central part of the PN. Fig. 1 (panels b and c) shows the slit views for M 1-42. For Hf 2-2, there are two exposures: a 30 min exposure with a slit width of 2 arcsec and 15 min exposure with a slit width of 10 arcsec. The slit has a position angle of 45°, spanning from the central star to the bright condensation in the southwest. Fig. 1 (panels d and e) shows the slit views of Hf 2-2. The full width at half-maximum (FWHM) of the emission lines is $\sim$0.15–0.6 Å from the blue to the red part.

Spectra were reduced using the ESO software MIDAS[2]. The spectra were first de-biased, corrected for the flat field, and cosmic-ray removed. Wavelength calibration was then performed using exposures of arc lamps. We then flux-calibrated the spectra using the spectroscopic observations of the spectrophotometric standard stars CD -32° 9927, Feige 56, LTT 3864 and LTT 9293 (Hamuy et al. 1992, 1994). It is difficult to find a clear sky region in the 2D echelle spectra, therefore sky lines were removed manually. Due to the high spectral resolution, most of the lines do not suffer much from blending.

Considerable effort was devoted to sky subtraction. There were numerous skylines in the two-dimensional (2D) spectra, especially in the wavelength region beyond 5000 Å. Some skylines are blended with the nebular emission lines, complicating the data reduction. Sky subtraction on the 2D frames is not straightforward because no region on the slit could be defined as the sky background, as shown in Fig. 2, where the [S II] $\lambda\lambda$6716, 6731 nebular lines and the O II λ6721 recombination line are located. While emission lines in the blue region of the VLT UVES spectrum (mainly from 3000 to 5000 Å) suffer less from the contamination by skylines, the red part (from 5000 to 11 000 Å) are littered with the skylines. In order to remove the them, we first need to measure their widths and determine the central wavelengths. The weak and rich emission lines within the blue region also made skyline-locating fairly difficult, especially when the nebular expansion affects the profiles of the emission lines and a skyline is totally embedded in the emission feature. Despite the difficulties in skyline removal, we have developed the IDL routines to solve this problem.

Skylines that are not blended with any nebular emission lines were simply removed and replaced with local background continuum. Skylines that are completely blended with nebular lines are difficult to remove. These skylines were removed by fitting the unaffected region of the emission line with a polynomial and extrapolated to the whole slit, assuming the emission line has a symmetric profile. Any residual skylines after the subtraction only occur at either end of the CCD frame, where the detector efficiencies are low. For those sky lines utterly embedded in the relatively bright nebular lines, subtraction is impossible. Removal of these skylines will create artificial uncertainties in nebular line fluxes. Fortunately, these skylines do not affect the analysis of the most critical nebular emission lines.

Fig. 2 shows an example of sky subtraction for the spectrum of Hf 2-2 in the range 6649–6760 Å. The upper panel of the figure shows the spectrum before sky subtraction and the lower panel shows the spectrum after subtraction. We identified and removed about 900 skylines in the red region for NGC 6153, $\sim$800 for M 1-42 and $\sim$1200 for Hf 2-2. The skyline subtraction for the long-exposure spectra of NGC 6153, M 1-42 and Hf 2-2 are generally satisfactory, whereas a few remain in the short-exposure spectra due to the relatively low S/N.

[1] http://www.eso.org/sci/facilities/paranal/instruments/uves/index.html

[2] MIDAS is developed and distributed by the European Southern Observatory.

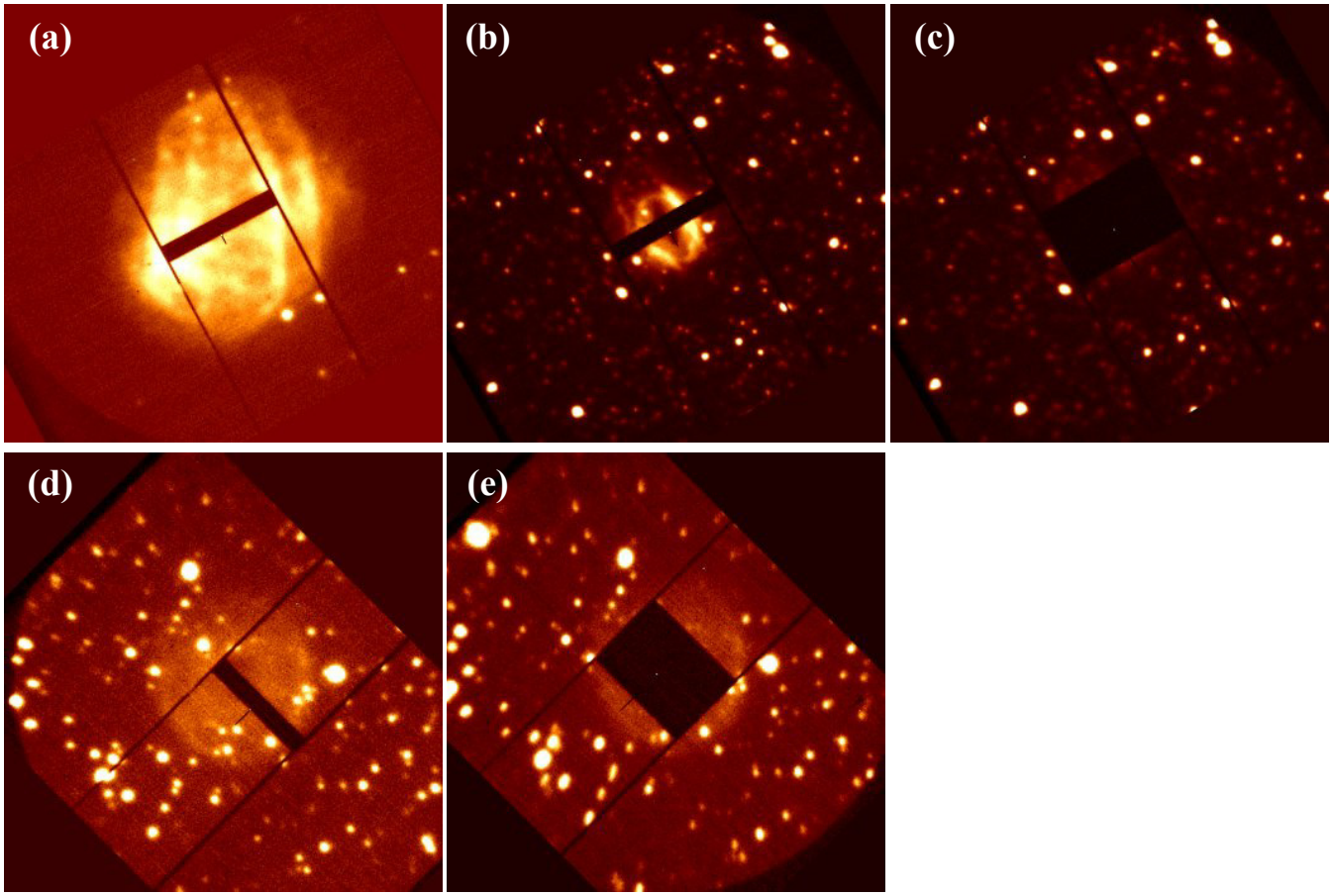

Figure 1. Slit views of NGC 6153 (panel a), M 1-42 (panels b and c), and H 2-2 (panels d and e). The overlaid slit widths are 2 arcsec for NGC 6153, and 2 arcsec and 10 arcsec for both M 1-42 and Hf 2-2. The field of view of each panel is roughly 40 arcsec × 40 arcsec. North is up and east to the left.

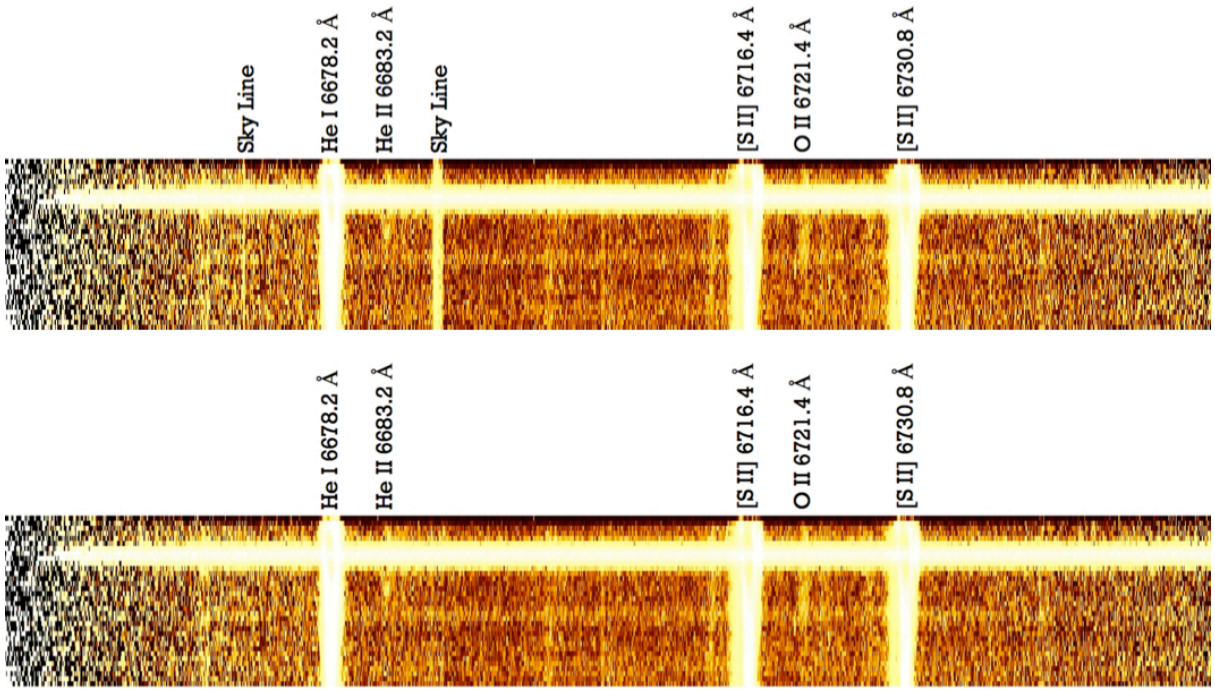

Figure 2. UVES 2D spectrum of Hf 2-2 (30 min exposure) from 6649 to 6760 Å. The top panel shows the spectrum before sky subtraction and the bottom panel shows the same section after sky subtraction. Emission lines are identified and labeled, including two sky lines.

Table 1. Journal of observations.

Object	Exp. Time (min)	Dichroic	Cross Disperser	Wave. Range (nm)	Slit Length (arcsec)	Pixel Scale (arcsec/pixel)
NGC 6153	20	DIC1	CD#1	303–388	10	0.25
		DIC2	CD#3	373–499	10	0.18
		DIC1	CD#2	476–684	13	0.25
		DIC2	CD#4	660–1060	13	0.17
	2	DIC1	CD#1	303–388	10	0.25
		DIC2	CD#3	373–499	10	0.18
		DIC1	CD#2	476–684	13	0.25
		DIC2	CD#4	660–1060	13	0.17
M 1-42	30	DIC1	CD#1	303–388	10	0.25
		DIC2	CD#3	373–499	10	0.18
		DIC1	CD#2	476–684	13	0.25
		DIC2	CD#4	660–1060	13	0.17
	15	DIC1	CD#1	303–388	10	0.25
		DIC2	CD#3	373–499	10	0.18
		DIC1	CD#2	476–684	13	0.25
		DIC2	CD#4	660–1060	13	0.17
	1	DIC1	CD#1	303–388	10	0.25
		DIC2	CD#3	373–499	10	0.18
		DIC1	CD#2	476–684	13	0.25
		DIC2	CD#4	660–1060	13	0.17
Hf 2-2	30	DIC1	CD#1	303–388	10	0.25
		DIC2	CD#3	373–499	10	0.18
		DIC1	CD#2	476–684	13	0.25
		DIC2	CD#4	660–1060	13	0.17
	15	DIC1	CD#1	303–388	10	0.25
		DIC2	CD#3	373–499	10	0.18
		DIC1	CD#2	476–684	13	0.25
		DIC2	CD#4	660–1060	13	0.17

3 THE 1D SPECTRA

The 1D spectra extracted from the cleaned 2D frames are presented in Fig. A1. Fig. 3 shows the ORLs of the O II M1 3p ^{4}D^o – 3s ^{4}P multiplet. Line fluxes were then measured by integration over the emission line profiles. Emission of the central stars was excluded in the spectrum extraction. Nebular expansion was clearly seen from the splitting of emission line profiles. Peaks of the two components can not be well-fitted with Gaussian profiles, therefore we integrated to get the total fluxes of each line. The extinction parameter $c(\mathrm{H}\beta)$ was derived from the observed H I Balmer line ratios, which were compared with the theoretical Case B ratios of Storey & Hummer (1995) assuming T_e = 10 000 K and N_e = 10^4 cm^{-3}.

For NGC 6153, we derived a $c(\mathrm{H}\beta)$ value of 1.32, as averaged from the $c(\mathrm{H}\beta)$ values derived from several Balmer line ratios. For M 1-42, our long-exposure (30 min) spectrum yield a $c(\mathrm{H}\beta)$ value of 0.699. The medium-exposure (15 min) spectrum yield a $c(\mathrm{H}\beta)$ value of 0.663, and the short-exposure (1 min) spectrum yield a $c(\mathrm{H}\beta)$ value of 0.779. Liu et al. (2001) derived a $c(\mathrm{H}\beta)$ of 0.70 for NGC 6153, which well agrees with our measurements of the long-exposure data. For Hf 2-2, measurements of the long-exposure (30 min) spectrum yield $c(\mathrm{H}\beta)$ = 0.361, while measurements of the medium-exposure (15 min) spectrum yield a $c(\mathrm{H}\beta)$ value of 0.439. Liu et al. (2006) derived $c(\mathrm{H}\beta)$ = 0.47 for Hf 2-2. The small differences between our extinction values and the literature probably arise from the different nebular regions sampled as well as the measurement errors. The error contribution from flux calibration is expected to be very small. The line fluxes were extinction corrected using

$$I(\lambda) = 10^{c(\mathrm{H}\beta)f(\lambda)}F(\lambda). \quad (1)$$

Here $f(\lambda)$ is the standard Galactic extinction curve for $R = 3.1$ (Cardelli, Clayton & Mathis 1989). The $c(\mathrm{H}\beta)$ values derived from the long-exposure (20 and 30 min) data were accurate and thus adopted in the extinction correction.

4 LINE IDENTIFICATIONS

After sky subtraction and extraction of the 1D spectra, we measured wavelengths and fluxes of the emission lines, and carried out emission line identification, following the procedure of Fang & Liu (2011). Table 2 presents the deep spectra of NGC 6153, M 1-42 and Hf 2-2, and will be available in its complete form as the online data. Generally there are two steps in emission line identification: (1) We first identified the emission lines manually, using the empirical method based on the available atomic transition database. Emission line lists from the literature (Sharpee et al. 2003; Zhang et al. 2005a; Fang & Liu 2011) were also used as references. Thanks to the high-spectral resolution, the majority of the important nebular emission lines seldom suffer from line blending. For the nebular lines with double peaks (due to nebular expansion), the average wavelength of the two components were used in line identification. (2) After a

Table 2. Emission lines detected in the long-exposure spectra of NGC 6153, M 1-42 and Hf 2-2. The observed line fluxes and the extinction-corrected intensities are normalized such that Hβ = 100. This is a sample of the complete table, which is available online only.

	NGC 6153			M 1-42			Hf 2-2								
	20 minutes			30 minutes			30 minutes								
λ_{lab} (Å)	$F(\lambda)$	$I(\lambda)$	Error (%)	$F(\lambda)$	$I(\lambda)$	Error (%)	$F(\lambda)$	$I(\lambda)$	Error (%)	ID	Mul.	Lower	Upper	g_1	g_2
3047.56	1.86	9.61	8.07	1.66	3.95	5.44				Ne II	V8	3p 4P*	3d 4D	4	6
3121.64	1.07	4.96	10.19	0.84	1.89	4.14				O III	V12	3p 3S	3d 3P*	3	3
3132.79	12.39	56.29	3.07	13.64	30.38	1.96	7.46	11.28	10.25	O III	V12	3p 3S	3d 3P*	3	5
3149.09				1.03	2.26	1.86				Ne II		3d 2F	5f 2¡3¿*	6	8
3187.74	2.41	10.07	1.95	2.41	5.14	1.95	9.19	13.58	2.91	He I	V3	2s 3S	4p 3P*	3	9
3203.17	2.89	11.81	2.53	3.46	7.28	0.32	4.44	6.52	7.61	He II	3.5a	3d 2D	5f 2F*	6	8
3218.19	1.00	4.00	9.22				4.96	7.24	14.69	Ne II	V13	3p 4D*	3d 4F	8	10
3229.55	1.04	4.11	24.10				5.52	8.03	2.50	Si II		3d′ 2P*	4f′ 2D	4	6
3230.54				1.57	3.23	21.15				N II		3D	3P*	7	5
3244.10	0.72	2.79	12.85	0.73	1.49	1.58	3.63	5.25	3.53	Ne II	V13	3p 4D*	3d 4F	6	8
3258.56				0.91	1.84	19.45	3.94	5.67	0.31	[Mn II]		a7S	a3H	7	11
3260.85	0.74	2.79	15.01	0.80	1.62	13.89				O III	V8	3p 3D	3d 3F*	5	7
3265.32	0.70	2.62	19.77							O III	V8	3p 3D	3d 3F*	7	9
3267.20							5.24	7.52	2.26	O III	V8	3p 3D	3d 3F*	3	5
3277.35				0.63	1.26	11.62				Fe II]	V1	a4D	z6D*	8	10
3289.98				0.68	1.34	15.86				O II	V23	3p 4P*	4s 4P	2	4
3299.40	1.22	4.41	3.52	1.13	2.23	2.35				O III	V3	3s 3P*	3p 3S	1	3
3304.31				0.72	1.41	13.24				Fe III		2S 4s3S	4D 4p3P*	3	5
3312.32	1.95	6.95	3.67	2.01	3.93	1.32				O III	V3	3s 3P*	3p 3S	3	3
3322.53				0.74	1.44	10.23				[Fe III]		5D	7S	9	7
3334.84	0.93	3.23	4.82	1.03	1.99	2.74	3.53	4.96	10.84	Ne II	V2	3s 4P	3p 4D*	6	8
3340.76	2.49	8.63	3.64	2.61	5.04	1.42	3.75	5.27	6.80	O III	V3	3s 3P*	3p 3S	5	3
3342.44	0.74	2.56	25.96	0.66	1.27	2.33	2.93	4.11	2.70	[Ne III]		2p4 1D	2p4 1S	5	1
3355.02	0.99	3.37	3.90	0.92	1.77	7.80	4.06	5.68	0.68	Ne II	V2	3s 4P	3p 4D*	4	6
3360.60	0.66	2.23	0.43	0.64	1.23	17.26				Ne II	V2	3s 4P	3p 4D*	1	3
3367.22	1.31	4.42	0.79	0.73	1.38	8.75				Ne II	V20	3p 2D*	3d 2F	6	8
3390.55				0.73	1.38	19.01				Ne II	V12	3p 4D*	3d 4D	2	4
3405.71	0.84	2.76	1.89							O III	V15	3p 3P	3d 3P*	1	3
3408.12	0.82	2.68	0.56							O III	V15	3p 3P	3d 3P*	3	1
3416.91				0.87	1.61	6.21				Ne II	V21	3p 2D*	3d 2D	6	6
3417.69	0.95	3.07	1.59				4.04	5.57	0.45	Ne II	V19	3p 2D*	3d 4F	6	8
3428.62	1.41	4.52	3.62	1.25	2.33	1.91				O III	V15	3p 3P	3d 3P*	3	5
3430.57	0.88	2.82	12.86							O III	V15	3p 3P	3d 3P*	5	3
3444.06	5.00	15.89	3.33	4.72	8.69	2.11	4.37	5.99	5.85	O III	V15	3p 3P	3d 3P*	5	5
3447.59	0.99	3.13	10.99	0.90	1.65	1.28	3.83	5.24	2.21	He I	V7	2s 1S	6p 1P*	1	3
3456.86	0.85	2.66	19.35							He I		2p 3P*	19d 3D	9	15

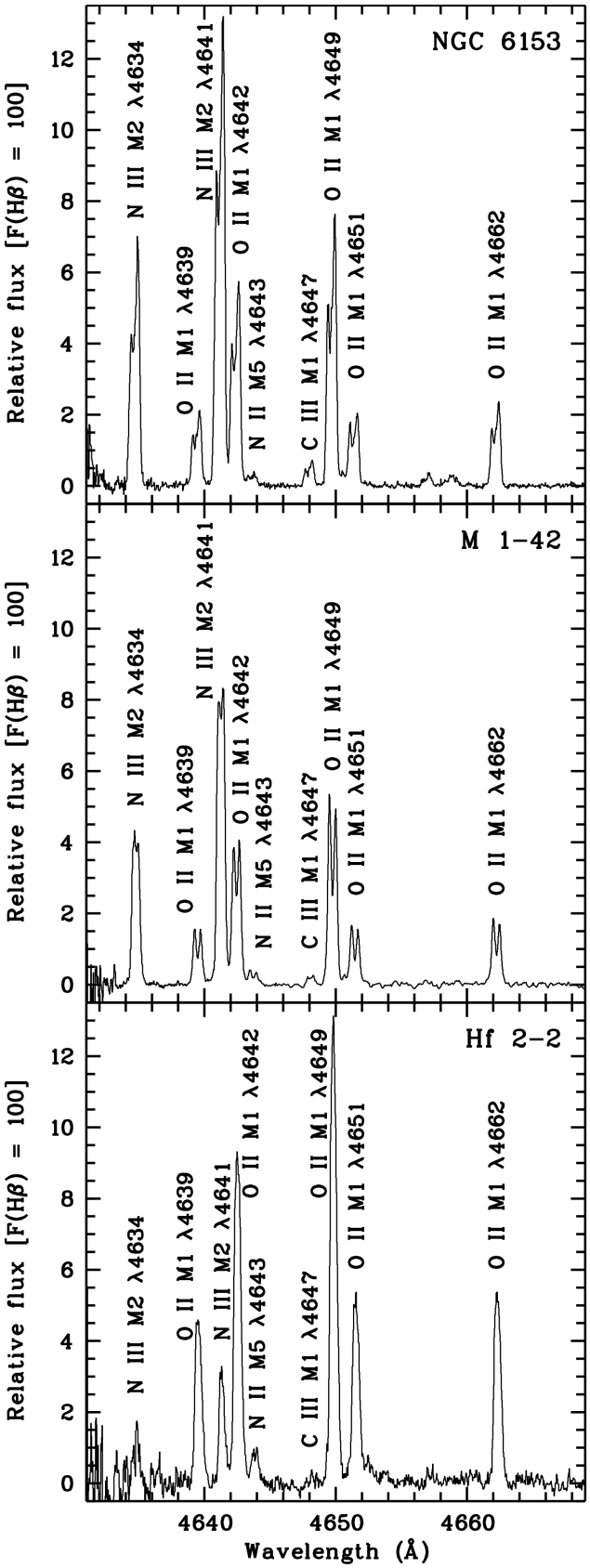

Figure 3. 1D spectra of NGC 6153 (top), M1 42 (middle) and Hf 2-2 (bottom) from 4631 Å to 4669 Å, showing the ORLs of the O II M1 $3p\,^4D^o$ – $3s\,^4P$ multiplet. Note the double-peak line profiles due to nebular expansion. Continuum has been subtracted from all three spectra. Extinction has not been corrected for.

complete (also preliminary) line list was constructed, it was used as an input file for the EMILI[3] code running for further identification.

Our line identification was first based on the observed wavelengths compared with the laboratory or theoretical wavelengths. We also checked the observed relative line fluxes against the predicted ones where available. The atomic transition tables compiled by Hirata & Horaguchi (1995) as well as the line lists of Galactic PNe IC 418 (Sharpee, Baldwin & Willams 2004), NGC 7027 (Zhang et al. 2005a), NGC 7009 (Fang & Liu 2011) were used in the line identification. For some features that we were unable to assign reasonable identifications, we used the online atomic transition database[4] as an aid. This empirical identification might be wrong for some faint lines. Once the EMILI runs were completed, we carefully checked the line lists for possible misidentifications. The correctness of line identifications was confirmed by searching for the fine-structure lines within a given multiplet of transition.

About 470 emission lines were identified in the long-exposure (20 min) spectrum of NGC 6153, whereas 240 lines were identified in the short-exposure (2 min) spectrum. About 330 emission lines were identified in the long-exposure (30 min) spectrum of M 1-42, whereas 320 lines were identified in the intermediate-exposure (15 min) and 150 in the short-exposure (1 min) spectrum. 310 emission lines were identified in the long-exposure (30 min) spectrum of Hf 2-2, and 290 in the medium-exposure (15 min). The emission line tables of the deep spectra of the three PNe are presented in Table 2 (the complete table is available as the online data). Fig. 4 shows the intensity distributions of the collisionally excited lines and the permitted lines identified in NGC 6153, M 1-42 and Hf 2-2. These permitted lines are emitted by the most abundant heavy element ions (C II, N II, O II and Ne II). Fig. 5 shows the histograms of the intensities of all emission lines identified in the deep spectra of the three PNe. Numbers of the ORLs of different ions are also presented.

5 PLASMA DIAGNOSTICS

Electron temperatures and densities of NGC 6153, M 1-42 and Hf 2-2 were deduced using the CEL and ORL ratios of heavy elements detected in the spectra of the three PNe. Electron temperatures can also be derived from the hydrogen recombination continuum discontinuities (Zhang et al. 2004), the Balmer jump at 3646 Å and the Paschen jump at 8204 Å. Electron densities can be constrained using the high-order Balmer and Paschen decrements (e.g., Liu et al. 2000). The He I recombination line ratios can also be used as temperature diagnostics (Zhang et al. 2005b). Recombination may enhance the most commonly used temperature-sensitive [N II], [O II] and [O III] auroral lines (Liu et al. 2000). This possibility is discussed below, with the amounts of enhancements estimated.

5.1 Plasma diagnostics based on CELs

CELs are the traditional tools for plasma diagnostics and abundance determinations. Numerous CELs were detected in the echelle spectra of NGC 6153, M 1-42 and Hf 2-2. We derived physical

[3] EMILI was originally developed by Sharpee et al. (2003) and was used to identify weak emission lines, particularly the weak recombination lines detected in deep, high-dispersion spectra.

[4] Atomic Line List v2.05 by P. A. M. van Hoof, website: http://www.pa.uky.edu/∼peter/newpage/

Table 3. References for atomic data.

Ion	Collisionally excited lines	
	Transition probabilities	Collision Strengths
[N I]	Zeippen (1982)	Berrington & Burke (1981)
[N II]	Nussbaumer & Rusca (1979)	Stafford et al. (1994)
[N III]	Fang, Kwong & Parkinson (1993)	Blum & Pradhan (1992)
[O II]	Zeippen (1982)	Pradhan (1976)
[O III]	Nussbaumer & Storey (1981)	Aggarwal (1983)
[Ne III]	Mendoza (1983)	Butler & Zeippen (1994)
[S II]	Mendoza & Zeippen (1982)	Keenan et al. (1996)
	Keenan et al. (1993)	
[S III]	Mendoza & Zeippen (1982)	Mendoza (1983)
[Cl III]	Mendoza (1983)	Mendoza (1983)
[Ar III]	Pelan & Berrington (1995)	Vujnovic & Wiese (1992)
[Ar IV]	Mendoza & Zeippen (1982)	Butler & Zeippen (1989)

Ion	Optical recombination lines	
	Effective recomb. coeffs.	Case
H I	Storey & Hummer (1995)	B
He I	Benjamin, Skillman & Smits (1999)	B: singlets
	Brocklehurst (1972)	A: triplets
He II	Storey & Hummer (1995)	B
C II	Davey, Storey & Kisielius (2000)	A
N II	Fang, Storey & Liu (2013)	B
N III	Péquignot, Petitjean & Boisson (1991)	A
	Nussbaumer & Storey (1984)	
O II	Storey (unpublished)	B
O III	Péquignot, Petitjean & Boisson (1991)	A
Ne II	Kisielius et al. (1998)	B: doublets
	Storey (unpublished)	Case A: quartets
	Nussbaumer & Storey (1987)	Dielectronic recombination

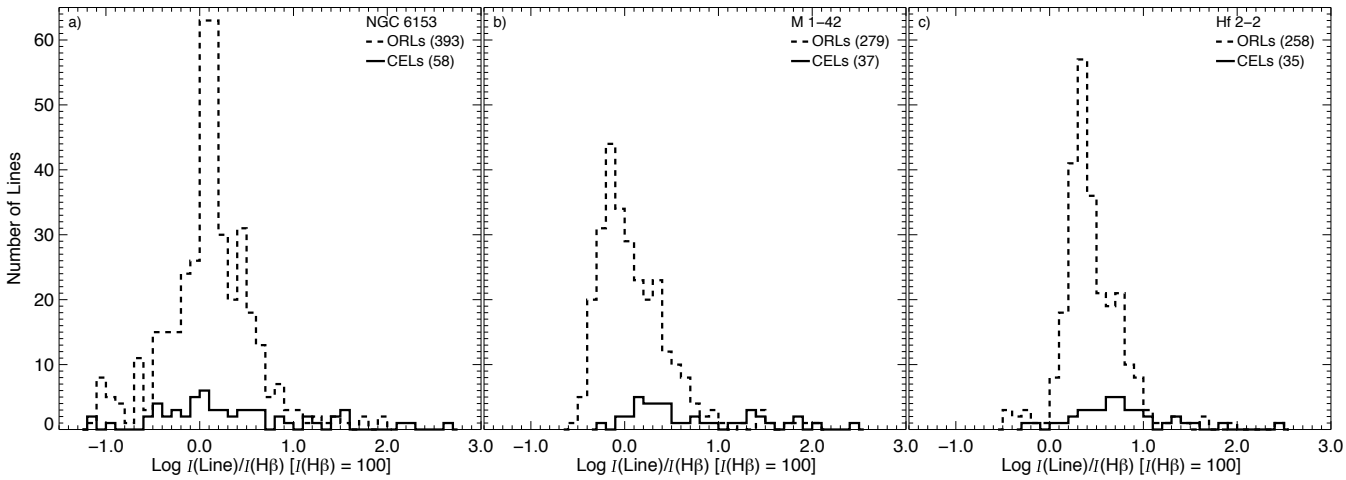

Figure 4. Number distributions of the ORL (dashed lines) and CEL (solid lines) intensities for the long-exposure data of NGC 6153 (a), M 1-42 (b), and Hf 2-2 (c).

properties (electron temperatures and densities) and then derived ionic abundances using the fluxes of the CELs measured in the spectra. This analysis was carried out with the aid of the EQUIB code, which was originally developed by Howarth & Adams (1981) to solve the equations of statistical equilibrium in multi-level atoms in nebular conditions. The atomic data used by the EQUIB code were updated manually. References for the atomic data set used for plasma diagnostics based on CELs, as well as for ionic abundance determinations, are presented in Table 3. Results of our plasma diagnostics are presented in Table 4. Discussion of the physical conditions yielded by our plasma diagnostics is presented in Section 7.2.

The electron temperatures were derived by assuming a constant electron density, which is averaged from the densities derived from the [O II], [Cl III] and [Ar IV] line ratios. The temperatures that are either too low or too high were not included in the average calculation. The [O I] (λ6300 + λ6363)/λ5577 temperature diag-

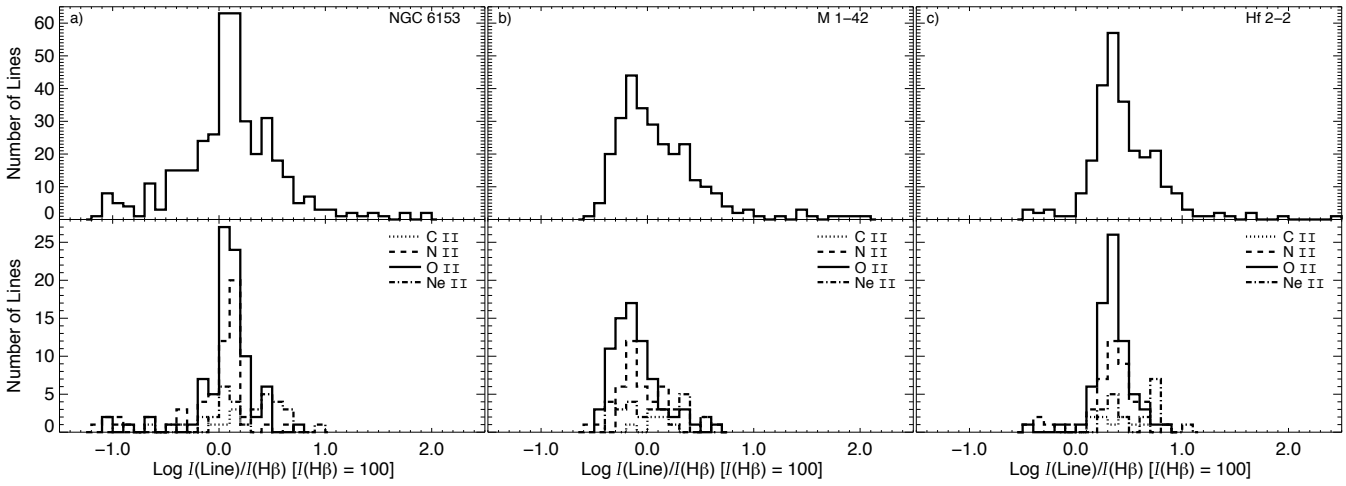

Figure 5. Number distributions of emission line intensities of NGC 6153 (left), M 1-42 (middle) and Hf 2-2 (right). The upper panels show the intensity distribution of all emission lines, and the lower panels show the distribution of the C II, N II, O II, and Ne II ORLs.

nostic ratio is not used because of possible residuals from the sky subtraction.

Fig. 6 shows the plasma diagnostic curves based on the CEL ratios measured in the long-exposure spectra of NGC 6153, M 1-42 and Hf 2-2. As previously mentioned, the [N II], [O II] and [O III] auroral lines could be enhanced by the recombination process. The diagnostic curves derived for these three ions before and after correction for the recombination contribution are represented with different line types in Fig. 6 (see the figure caption for details). If a PN has uniform physical condition, the electron temperatures and densities derived from different diagnostics ratios should be confined within a narrow region in the diagram. These curves do not intersect at a single point, indicating the temperature and density inhomogeneity in the three PNe (e.g., Kwok 2000).

5.2 Enhancement of the [N II], [O II] and [O III] auroral lines by recombination excitation

In NGC 6153, M 1-42 and Hf 2-2, the nitrogen and oxygen atoms are mostly in their doubly-ionized stages, N^{2+} and O^{2+}. Recombination of the N^{2+} and O^{2+} ions (to N^{+} and O^{+}, respectively) may contribute to the excitation of the weak [N II] λ5754 auroral line and the [O II] auroral $\lambda\lambda$7320,7330 and nebular $\lambda\lambda$3726,3729 lines (Liu et al. 2000). This could result in the overestimated electron temperatures derived from the (λ6548 + λ6584)/λ5754 and (λ7320 + λ7330)/λ3727 line ratios (Rubin 1989). Similarly, recombination could also enhance the [O III] λ4363 auroral line, thereby leading to an overestimated electron temperature. We estimated the contribution by recombination using the empirical fitting formulae of Liu et al. (2000, Equations 1, 2 and 3 therein), which were derived from the atomic data of N^{+}, O^{+} and O^{2+}.

We estimated that recombination only contributes less than 1 per cent to the total intensity of the [N II] λ5754 auroral line. Here we used an N^{2+}/H^{+} recombination line abundance of 1.75×10^{-3} for NGC 6153 (Liu et al. 2000), 2.86×10^{-3} for M 1-42 (Liu et al. 2001) and 2.72×10^{-3} for Hf 2-2 (Liu et al. 2006). For the O^{2+}/H^{+} recombination line abundance, we adopted a value of 4.07×10^{-3} for NGC 6153 (Liu et al. 2000), 5.59×10^{-3} for M 1-42 (Liu et al. 2001), and 7.48×10^{-3} for Hf 2-2 (Liu et al. 2006). For the O^{3+}/H^{+} recombination line abundance, we adopted 2.37×10^{-4} for NGC 6153 (Liu et al. 2000), 3.26×10^{-4} for M 1-42 (Liu et al. 2001), and 4.35×10^{-4} for Hf 2-2 (Liu et al. 2006). Here we adopted the average temperatures deduced from CEL diagnostic ratios listed in Table 4 to calculate the contribution by recombination. The corrected electron temperatures were then used to derive an average value, which was adopted in the abundance calculations.

5.3 Plasma diagnostics based on the H I recombination spectrum

Table 4 presents plasma diagnostic results based on the hydrogen recombination spectrum. These temperatures were derived from the intensity ratio of the nebular continuum at Balmer jump (3646 Å) to the H11 λ3770 line, defined as $[I_{\rm c}(\lambda3643) - I_{\rm c}(\lambda3681)]/I({\rm H11})$, where $I_{\rm c}(\lambda3643)$ and $I_{\rm c}(\lambda3681)$ are intensities of the nebular continua at 3643 Å and 3681 Å, respectively. We derived the Balmer jump temperature using the fitting formula given by Liu et al. (2001, Equation 3 therein). Our Balmer jump diagnostics are generally consistent with those of Zhang et al. (2004).

The intensity ratios of high-order $I(n\rightarrow2,\ n\ \geqslant10)$ Balmer lines relative to Hβ are sensitive to the electron density but insensitive the electron temperature (Zhang et al. 2004). This diagnostic works well for the high-density plasmas ($N_{\rm e}\ \geqslant10^{6}$ cm^{-3}; Liu et al. 2000). The Balmer lines in our deep UVES spectra can be resolved up to n=24. For even higher-n Balmer lines, measurements of line fluxes become unreliable due to possible line blending. Fig. 7 shows the Balmer line intensities relative to Hβ as a function of n ($10\leqslant n\leqslant24$) for NGC 6153, M 1-42 and Hf 2-2. For M 1-42, there were fewer Balmer lines detected in the spectra due to the low S/N ratio. Not only the H14 and H16 are overestimated due to line blending, but some other high-order Balmer lines might also be affected, as shown in Fig. 7. Also over-plotted in the Fig. 7 are the theoretical Balmer decrements at different electron densities at the electron temperature deduced from the Balmer jump. The theoretical relative intensities of Balmer lines were calculated from the Case B emissivities of H I lines (Storey & Hummer 1995). The electron densities yielded by a least-squares optimization are presented in Table 4.

Electron temperature can also be diagnosed from the Paschen jump around 8204 Å (e.g., Fang & Liu 2011, Equation 7 therein). The fitting errors introduced by this formula are less than 5 per cent in the range $3500\leqslant\ T_{\rm e}\ \leqslant14\,000$ K, and are less than 16 per cent

Table 4. Plasma diagnostics.

ID	Diagnostic	Results					
		T_e (K)					
		NGC 6153		M 1-42		Hf 2-2	
		20 minutes*	Literature[a]	30 minutes*	Literature[b]	30 minutes*	Literature[c]
1	[N II] (λ6548+λ6584)/λ5754	10550^{100}_{150}	10200	10000^{750}_{1000}	8900	12500^{400}_{350}	14500
2	[O III] (λ4958+λ5007)/λ4363	9850^{350}_{400}	9100	8900^{300}_{300}	9200	9650^{450}_{400}	8700
3	[S III] (λ9069+λ9531)/λ6312	17050^{500}_{600}	9100	14750^{1000}_{1500}	9200	11250^{1000}_{1000}	8700
4	[O II] (λ7320+λ7330)/(λ3726 + λ3729)	11800^{4550}_{1000}	17900[d]	14000^{2000}_{2000}	16850	13200^{1000}_{1001}	
5	[Ar III] (λ7135+λ7752)/λ5192	9350^{500}_{250}	9200[e]	18900^{650}_{600}	7100[e]		
6	[S II] (λ6717+λ6731)/(λ4069+λ4076)[f]	11850^{1500}_{500}		5500^{1500}_{1000}		9250^{1000}_{1000}	
	Average CEL temperature	11750±2800	11600±4200	12050±4800	10200±3400	11200±1750	11600±4000
7	[Ne III] (λ3868+λ3967)/λ3342	25400^{3650}_{3600}	8600[g]	24450^{2000}_{1750}	8800[g]	23000^{1500}_{1500}	
	He I λ7281/λ6678	3100^{450}_{400}		3100^{450}_{400}		3300^{550}_{350}	
	He I λ7281/λ5876	3800^{500}_{650}		3800^{500}_{650}		3400^{250}_{400}	
	He I λ6678/λ4471	3250^{350}_{450}		3250^{350}_{450}		2700^{400}_{250}	
	He I λ5876/λ4471	2900^{300}_{250}		2900^{300}_{250}		2750^{350}_{200}	
	H I BJ/H11	6250^{150}_{100}	6100	3450^{200}_{250}	3560	1050^{250}_{150}	930
	H I PJ/P11	2500^{500}_{650}		600^{150}_{200}		550^{300}_{250}	
		log N_e [cm^{-3}]					
		NGC 6153		M 1-42		Hf 2-2	
		20 minutes*	Literature[a]	30 minutes*	Literature[b]	30 minutes*	Literature[c]
8	[Ar IV] λ4740/λ4711	$3.71^{0.15}_{0.10}$	3.40	$3.82^{0.05}_{0.05}$	2.80	$4.18^{0.65}_{0.40}$	
9	[Cl III] λ5537/λ5517	$3.23^{0.10}_{0.05}$	3.60	$3.20^{0.05}_{0.15}$	3.20	$3.22^{0.15}_{0.25}$	
10	[S II] λ6731/λ6716[g]	$2.60^{0.25}_{0.40}$	3.60	$2.30^{0.40}_{0.05}$	3.10	$2.90^{0.10}_{0.05}$	2.60
11	[O II] λ3729/λ3726	$3.46^{0.10}_{0.10}$		$3.19^{0.05}_{0.05}$	3.20	$2.99^{0.15}_{0.10}$	3.20
	Average CEL density	3.47±2.43	3.50±0.10	3.40±3.59	3.00±0.20	3.46±6.27	2.90±0.30
12	[N I] λ5200/λ5198[h]	$2.88^{0.20}_{0.05}$		$2.87^{0.10}_{0.05}$		$2.70^{0.30}_{0.10}$	
	Balmer Decrement	$4.0^{0.75}_{0.50}$	3.3	$4.2^{0.35}_{0.60}$	$\leqslant$4.0	$5.0^{0.50}_{0.95}$	2.5
	Paschen Decrement	$4.0^{0.25}_{0.35}$		$4.5^{1.20}_{1.00}$		$4.2^{1.50}_{0.75}$	

*The super- and subscripts are the errors.

[a] Liu et al. (2000), observations of the entire nebula.

[b] Liu et al. (2001).

[c] Liu et al. (2006), 2 arcsec wide-slit spectroscopy.

[d] From the line ratio (λ7320+λ7330)/λ3727.

[e] From the line ratio λ7135/λ5192.

[f] The critical densities of the [S II] $\lambda\lambda$6716 and 6731 lines are only 1400 and 3800 cm^{-3}, respectively. Thus, at least the 6716 line could be suppressed by electron collisions, i.e. collisionally de-excited and the derived density could be unreliable.

[g] From the line ratio 15.5μm/(λ3868+λ3967).

[h] The critical densities of the [N I] $\lambda\lambda$5198 and 5200 lines are 1800 and 780 cm^{-3}, respectively. Thus, these two lines could be collisionally de-excited, i.e. suppressed by electron collisions.

at 3200$\leqslant$ T_e $\leqslant$25 000 K (Fang & Liu 2011). The derived Paschen jump temperatures are presented in Table 4 for NGC 6153, M 1-42 and Hf 2-2. Fig. 8 shows the relatively intensities of Paschen lines as a function of n for 11$\leqslant n \leqslant$23 measured from the deep spectra of NGC 6153, M 1-42 and Hf 2-2. Also over-plotted in Fig. 8 are the theoretical relative intensities of the Paschen lines as a function of the principle quantum number n at different electron densities. For M 1-42, same as the Balmer lines, there are fewer high-order Paschen lines that can be used to constrain the electron density. For Hf 2-2, measurements of the high-order Paschen lines have relatively large uncertainties due to faintness of this PN which produce relatively low S/N of the spectrum, yielding unreliable electron densities. Some high-order Paschen lines are stronger than the lower-order lines probably due to line blending. The electron temperatures derived from the Paschen jump, as given in Table 4, was assumed when calculating the theoretical curves of the Paschen decrements.

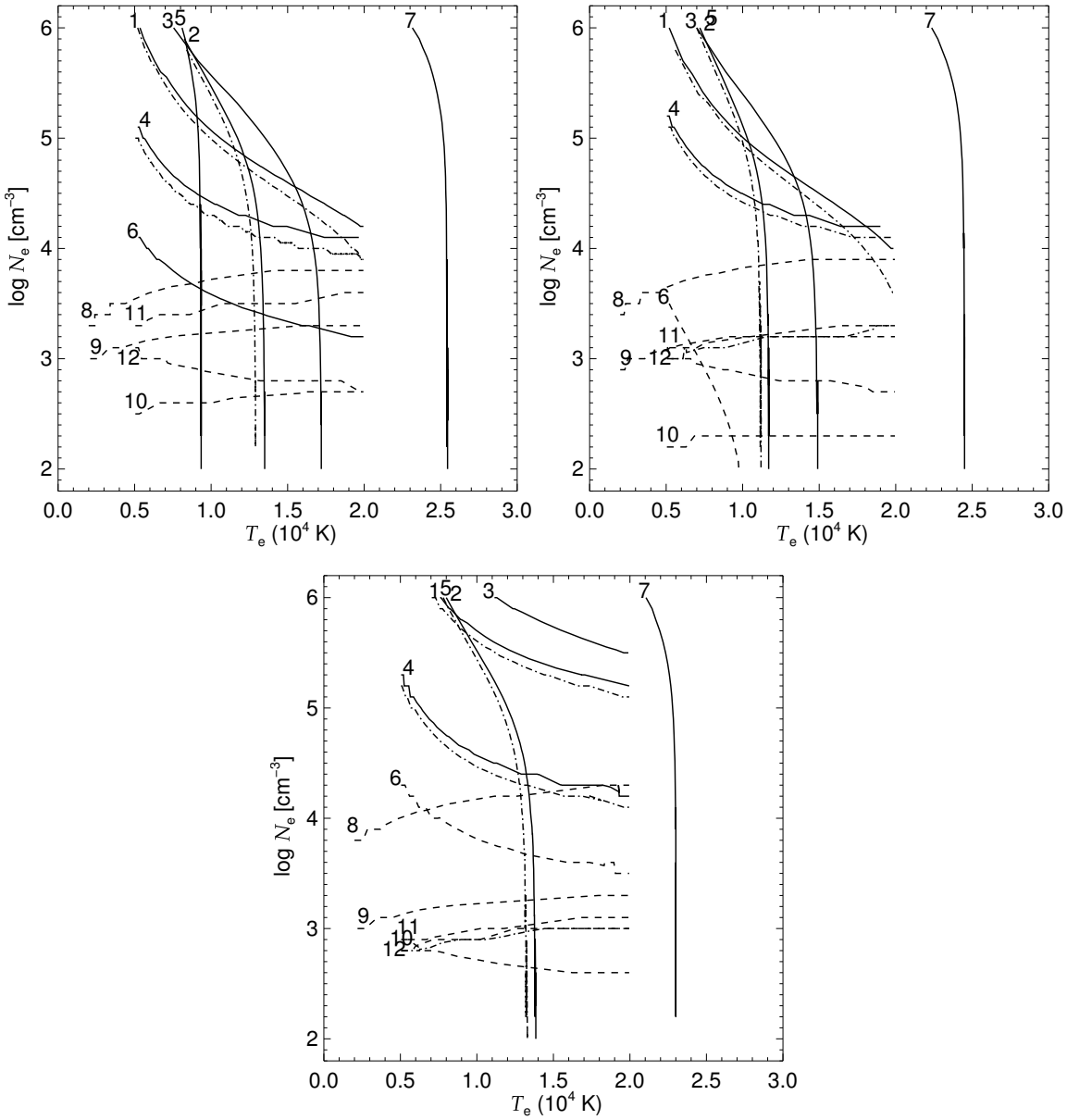

Figure 6. Plasma diagnostic diagrams for the long-exposure spectra of NGC 6153 (top-left panel), M 1-42 (top-right panel) and Hf 2-2 (bottom panel). Each curve is labeled with an ID number given in Table 4. The solid curves are the temperature diagnostics, and the dashed curves the density diagnostics. The dash-dot curves represent the temperature-diagnostic curves of [N II], [O II] and [O III] after correction of auroral line fluxes for the contribution from recombination excitation, and the solid curves represent those without corrections.

5.4 Temperature diagnostics based on the He I recombination spectrum

The temperature diagnostics based on the He I recombination line ratios have been developed by Zhang et al. (2005b), who adopted the theoretical He I line emissivities of Benjamin, Skillman & Smits (1999). Table 4 presents the electron temperatures diagnosed from the intensity ratios of the He I $\lambda\lambda$4471,5876,6678,7281 optical recombination lines for NGC 6153, M 1-42 and Hf 2-2. Here the analytical formula of (Zhang et al. 2005b, Equation 1 therein) was used to derived the temperatures. Equation 1 in Zhang et al. (2005b) is valid from 5000 K to 20 000 K. For the range T_e <5000 K, Zhang et al. (2005b) made analytical fits based on the theoretical He I line emissivities of Smits (1996) and the collisional data among low-n levels of Sawey & Berrington (1993). We derived electron temperatures from the He I λ7281/λ6678, λ7281/λ5876, λ6678/λ4471 and λ5876/λ4471 line ratios, as listed in Table 4. Since λ7281/λ6678 is the best diagnostic ratio of He I for temperature determination (Zhang et al. 2005b), we adopted the temperatures derived from this line ratio for all three PNe.

5.5 Plasma diagnostics based on the heavy element ORLs

In a low-density nebula, the relative populations of the lowest fine-structure levels of a recombining ion (e.g., N^{2+} $^2P^o_{1/2}$ and $^2P^o_{3/2}$ in the case of N II) vary with the electron density, resulting a density dependence of the relative line emissivities of the fine-structure lines belonging to a given multiplet of the recombined ion (Fang, Storey & Liu 2011). The intensity ratio of two ORLs of the same

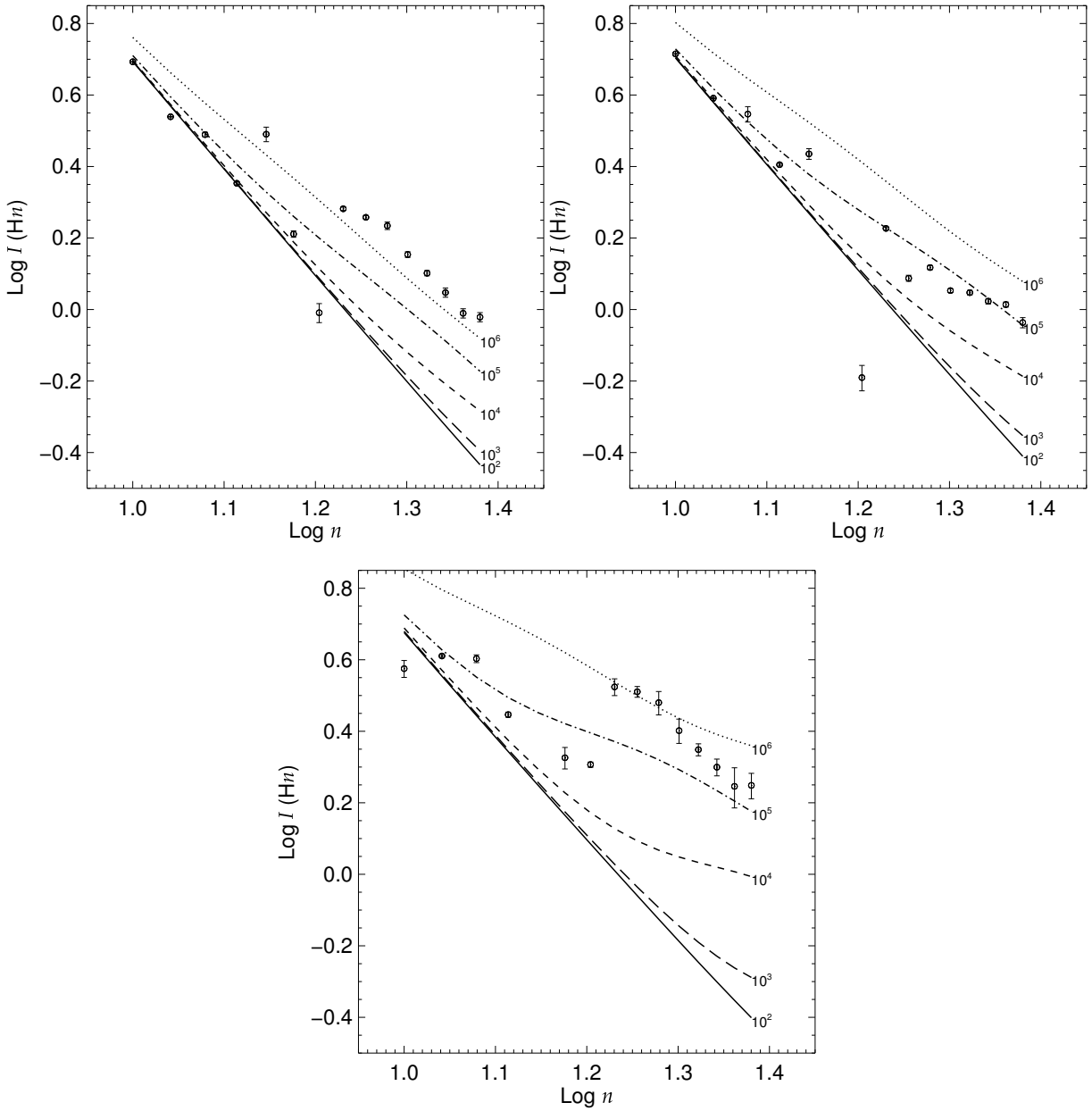

Figure 7. Observed intensities (normalized to Hβ = 100) of high-n (n = 10, 11, 12, ..., 24) Balmer lines as a function of the principal quantum number n for NGC 6153 (top-left panel), M 1-42 (top-right panel) and Hf 2-2 (bottom panel). Some of the high-order Balmer lines may be overestimated due to line blending. The curves are the predicted Balmer decrements for a number of density cases, from 10^2 to 10^6 cm^{-3}. The curves are created using the hydrogenic theory of Storey & Hummer (1995). The assumed electron temperatures are presented in Table 4 for NGC 6153, M 1-42 and Hf 2-2.

multiplet but coming from different parent levels (of the recombining ion) can be used to determine the electron density (Fang, Storey & Liu 2011). Under typical nebular conditions, the emissivity of an ORL has a weak, power-law dependence on the electron temperature. This weak temperature dependence differs for the ORLs that come from levels of different orbital angular momentum quantum numbers l. This difference is obvious if the two lines decay from levels with very different l. Therefore, using the intensity ratio of two ORLs with different l, we can determine the electron temperature, given that accurate measurements of ORLs are secured.

The electron temperatures and densities diagnosed from the N II and O II ORLs for the three PNe have been presented in McNabb et al. (2013, Table 1 and Figs 6 and 7). They utilized a least-squares fitting method that compares the theoretical intensities computed from the emissivities of the N II and O II ORLs over a broad range of $T_{\rm e}$ and $N_{\rm e}$ with the intensities found in the literature. Using a Monte Carlo-like method for generating simulated intensities within the observational errors, they were able to propagate those errors to the best-fit temperatures and densities for the N II and O II ORLs. Plasma diagnostics for NGC 6153, M 1-42 and Hf 2-2 using the N II and O II line ratios are presented in Figs 9, 10, 11 and 12. Generally the temperatures of the three PNe derived from the O II λ4649/λ4089 intensity ratio are all below 2500 K (Fig. 11), and the temperatures yielded by the N II λ5679/λ4041 line ratio are below 3000 K, except that of M 1-42 whose N II temperature is $\sim$8000 K (Fig. 9), much higher than the temperature

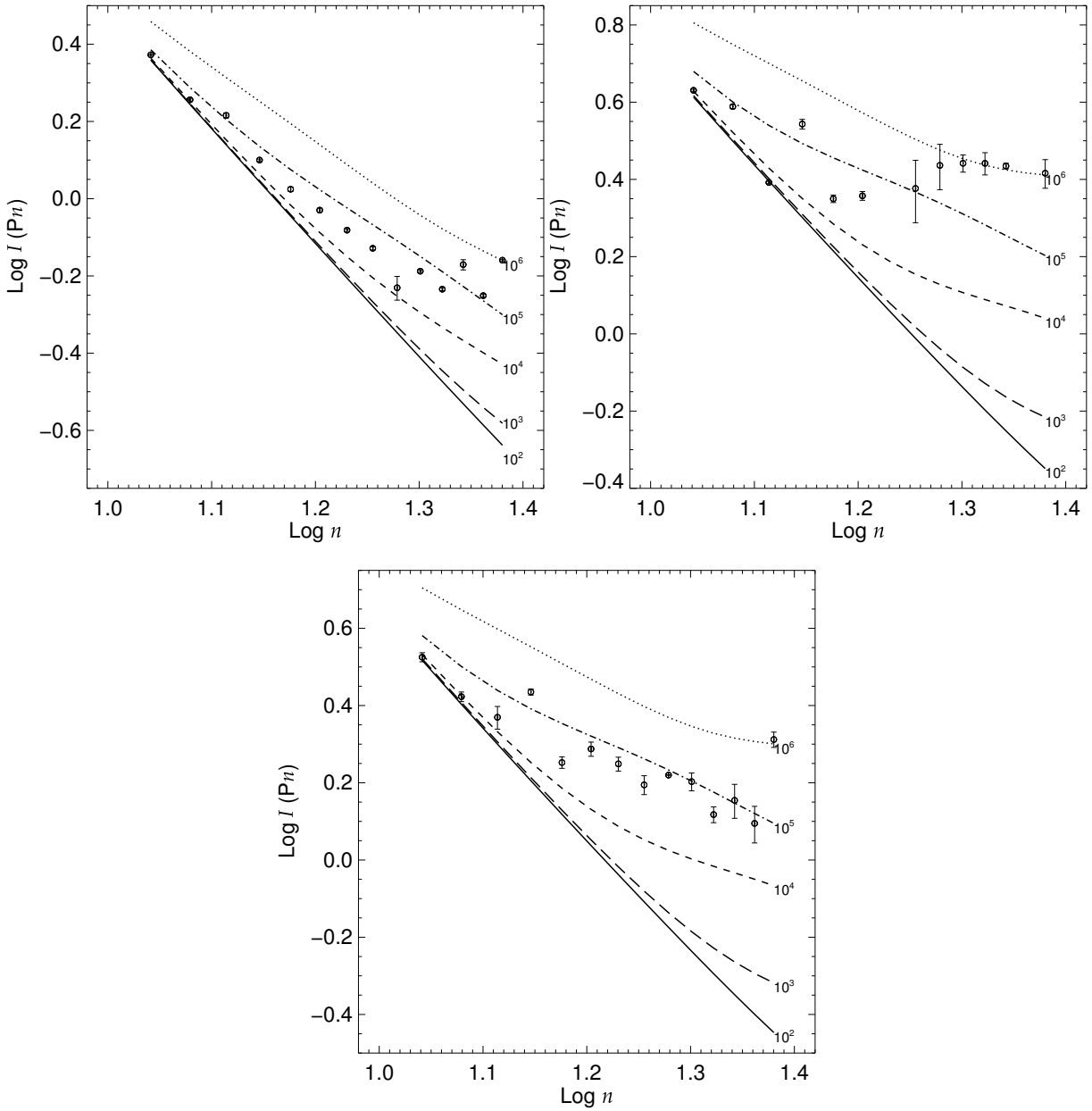

Figure 8. Observed intensities (normalized to Hβ = 100) of high-n (n = 11, 12, ..., 23) Paschen lines as a function of the principal quantum number n for NGC 6153 (top-left panel), M 1-42 (top-right panel) and Hf 2-2 (bottom panel). The intensities of P22, P23 and P24 may be overestimated due to line blending. The curves are the predicted Paschen decrements for a number of density cases, from 10^2 to 10^6 cm^{-3}. The assumed electron temperature is presented in Table 4 for NGC 6153, M 1-42 and Hf 2-2.

diagnosed by McNabb et al. (2013). The electron densities derived from the N II and O II line ratios have large uncertainties mainly due to the very weak density-dependence of the ORL line ratios.

6 ABUNDANCES

6.1 Ionic abundances from CELs

We have observed numerous forbidden lines of heavy element CELs, including [N I], [N II], [O I], [O II], [O III], [Ne III], [Ne IV], [S II], [S III], [Cl II], [Cl III], [Cl IV], [Ar III] and [Ar IV]. Ionic abundances were derived by solving population equations of multi-level atomic models. The CEL temperatures and densities in Table 4 were assumed in the abundance calculations.

$T_{\rm e}$[N II] is typically assumed for low-ionization species and $T_{\rm e}$[O III] for ions of higher ionization degrees. As discussed earlier, although electron temperatures derived from the [N II] and [O II] nebular-to-auroral line ratios can be overestimated due to recombination excitation (Rubin 1989; Liu et al. 2000) this effect is negligible in our spectra. Abundances of N^0, N^+, O^+, O^{++}, Ne^{++}, S^+, S^{++}, Cl^{++}, Ar^{++} and Ar^{3+} relative to hydrogen have been determined from CELs. We have adopted the average electron temperatures and densities derived from CELs. Ionic abundances are listed in Table 5 for NGC 6153, M 1-42 and Hf 2-2. For each ion that have multiple CELs detected, the adopted ionic abundance was

Table 5. CEL ionic abundances.

Ion	Spectrum	Lines Used	Abundances ($\times 10^{-5}$)					
			NGC 6153		M 1-42		Hf 2-2	
			20 minutes*	Literature[a]	30 minutes*	Literature[b]	30 minutes*	Literature[c]
N^0	[N I]	λλ5198.5200	$12.90^{(9.9)}_{(2.5)}$		$16.70^{(4.3)}_{(2.1)}$		$10.07^{(13.3)}_{(3.5)}$	
N^+	[N II]	λλ5755, 6548, 6583	$1.29^{(8.0)}_{(5.3)}$	1.24	$5.30^{(10.5)}_{(6.1)}$	5.86	$0.87^{(6.0)}_{(6.2)}$	0.97
O^+	[O II]	λλ3726+29, 7320+30	$2.88^{(3.2)}_{(3.9)}$	2.62	$4.24^{(4.3)}_{(5.5)}$	3.88	$2.74^{(6.4)}_{(10.1)}$	2.13
O^+	[O II]	λλ3726+29	$2.14^{(9.4)}_{(9.4)}$	2.62	$3.46^{(3.2)}_{(3.2)}$	3.88	$2.62^{(6.0)}_{(4.0)}$	2.13
O^{2+}	[O III]	λλ4363, 4959, 5007	$38.54^{(8.3)}_{(6.2)}$	43.30	$21.59^{(12.8)}_{(8.7)}$	24.90	$10.82^{(14.0)}_{(13.8)}$	10.50
Ne^{2+}	[Ne III]	λλ3342, 3869, 3968	$9.66^{(13.8)}_{(26.3)}$	14.40	$8.53^{(10.5)}_{(9.5)}$	9.62	$3.74^{(11.8)}_{(12.3)}$	3.60
S^+	[S II]	λλ4068+76, 6716+31	$0.05^{(1.1)}_{(3.3)}$	0.05	$0.13^{(1.9)}_{(0.9)}$	0.13	$0.05^{(4.0)}_{(0.8)}$	0.03
S^+	[S II]	λλ6716+31	$0.04^{(6.2)}_{(7.7)}$	0.05	$0.20^{(2.9)}_{(0.9)}$	0.13	$0.05^{(3.6)}_{(1.4)}$	0.03
S^{2+}	[S III]	λλ6312, 9069, 9532	$0.42^{(4.4)}_{(4.3)}$	0.46	$0.62^{(7.2)}_{(7.5)}$	0.47	$0.12^{(2.9)}_{(2.1)}$	0.12
Cl^{2+}	[Cl III]	λλ5517, 5537	$0.01^{(12.3)}_{(6.1)}$	0.01	$0.02^{(6.6)}_{(13.7)}$	0.01	$0.01^{(18.5)}_{(10.2)}$	
Ar^{2+}	[Ar III]	λλ5182, 7136, 7751	$0.23^{(14.9)}_{(4.9)}$	0.18	$0.18^{(3.9)}_{(2.0)}$	0.19		0.07
Ar^{3+}	[Ar IV]	λλ4711, 4740	$0.07^{(2.6)}_{(1.7)}$	0.06	$0.05^{(1.3)}_{(1.3)}$	0.04	$0.04^{(2.4)}_{(1.7)}$	

* Values in parentheses are the propagated uncertainties based on observational error (in per cent). The super- and subscripts are the errors added to and subtracted from the observed fluxes, respectively, and then corrected for extinction.

[a] Liu et al. (2000), the observations of the entire nebula.

[b] Liu et al. (2001).

[c] Liu et al. (2006), 2 arcsec wide-slit spectroscopy.

Table 6. Ionic and elemental abundances of helium.

He^{i+}/H^+	Line (Å)	Abundance					
		NGC 6153		M 1-42		Hf 2-2	
		20 minutes	Literature[a]	30 minutes	Literature[b]	30 minutes	Literature[c]
He^+/H^+	He I λ4471	$0.130^{(13.8)}_{(14.0)}$	0.123	$0.113^{(6.1)}_{(6.3)}$	0.142	$0.142^{(2.4)}_{(2.4)}$	0.102
He^+/H^+	He I λ5876	$0.109^{(12.3)}_{(12.4)}$	0.127	$0.148^{(5.3)}_{(5.3)}$	0.141	$0.116^{(4.4)}_{(4.4)}$	0.103
He^+/H^+	He I λ6678	$0.122^{(4.5)}_{(4.6)}$		$0.143^{(4.8)}_{4.6)}$	0.138	$0.095^{(12.6)}_{(13.8)}$	0.099
He^+/H^+	Mean	$0.120^{(10.2)}_{(10.3)}$	0.123	$0.135^{(5.3)}_{(5.4)}$	0.139	$0.117^{(4.4)}_{(4.6)}$	0.102
He^+/H^+	He I λ7281	$0.104^{(13.6)}_{(13.6)}$	0.133	$0.102^{(9.1)}_{9.5)}$	0.095	$0.106^{(7.6)}_{(7.8)}$	
He^{2+}/H^+	He II λ4686	$0.010^{(12.0)}_{(12.1)}$	0.011	$0.010^{(8.7)}_{(8.8)}$	0.009	$0.001^{(4.4)}_{(4.6)}$	0.002
He/H		$0.110^{(10.0)}_{(10.2)}$	0.134	$0.124^{(5.0)}_{(5.1)}$	0.148	$0.116^{(11.4)}_{(11.7)}$	0.104
		$\log\ N(\mathrm{X})/N(\mathrm{H}) + 12$					
He		$11.12^{(4.0)}_{(4.1)}$	11.13	$11.16^{(2.2)}_{(2.2)}$	10.92	$11.07^{(4.3)}_{(4.5)}$	11.02

[a] Liu et al. (2000), observations of the entire nebula.

[b] Liu et al. (2001).

[c] Liu et al. (2006), 2 arcsec wide slit spectroscopy.

* Values in parentheses are the propagated uncertainties based on observational error (in per cent). The super- and subscripts are the errors added to and subtracted from the observed fluxes, respectively, and then corrected for extinction.

averaged from those lines. The ionic abundances were derived by solving population equations of multi-level atomic models. Fortran code EQUIB was used in ionic abundance calculations. The CEL temperatures and densities in Table 4 were assumed in the calculations. The CEL ionic abundances are compared with the literature. Differences between our values and those in the literature can be explained by either the different instrumentation used or by the different analysis methodology implemented.

6.2 Ionic abundances from ORLs

We identified more than 200 permitted lines in the deep spectrum for each of the three PNe. These lines mainly come from the C, N,

Table 7. Recombination line C^{2+}/H^+ abundances for NGC 6153, M 1-42 and Hf 2-2. Intensities are normalized such that Hβ = 100. The effective recombination coefficients are from Davey, Storey & Kisielius (2000).

Line (Å)	Mult.	NGC 6153				M 1-42				Hf 2-2			
		20 minutes		Literature[a]		30 minutes		Literature[b]		30 minutes		Literature[c]	
		$\frac{I_{obs}}{I(H\beta)}$	C^{2+}/H^{+*} ($\times10^{-3}$)	$\frac{I_{obs}}{I(H\beta)}$	C^{2+}/H^+ ($\times10^{-3}$)	$\frac{I_{obs}}{I(H\beta)}$	C^{2+}/H^{+*} ($\times10^{-3}$)	$\frac{I_{obs}}{I(H\beta)}$	C^{2+}/H^+ ($\times10^{-3}$)	$\frac{I_{obs}}{I(H\beta)}$	C^{2+}/H^{+*} ($\times10^{-3}$)	$\frac{I_{obs}}{I(H\beta)}$	C^{2+}/H^+ ($\times10^{-3}$)
λ7231.32	M3	1.30	$0.74^{(5.1)}_{(5.2)}$	0.36	0.85	1.72	$0.98^{(1.5)}_{(1.5)}$	0.56	1.26	2.93	$1.67^{(3.0)}_{(3.0)}$		
M3 3d ^{2}D – 3p ^{2}P^o													
λ4267.38	M6	4.62	$2.26^{(2.5)}_{(2.5)}$	2.40	2.25	3.79	$3.72^{(2.0)}_{(2.1)}$	2.55	1.98	10.13	$3.31^{(4.0)}_{(4.0)}$	7.60	3.68
M6 4f ^{2}F^o – 3d ^{2}D													
λ6151.43	M16.04	0.71	$1.62^{(2.8)}_{(2.8)}$	0.08						1.92	$4.37^{(3.5)}_{(3.6)}$	0.08	
M16.04 6f ^{2}F^o – 4d ^{2}D													
λ9903.46	M17.02	0.45	$1.83^{(3.8)}_{(3.8)}$			1.13	$4.64^{(2.9)}_{(3.0)}$			1.39	$5.71^{(1.7)}_{(1.8)}$		
M17.02 5g ^{2}G – 4f ^{2}F^o													
λ6461.95	M17.04	0.68	$6.47^{(3.2)}_{(3.4)}$	0.25		1.05	$1.00^{(2.3)}_{(2.4)}$			2.35	$2.23^{(3.5)}_{(3.6)}$	0.74	3.21
M17.04 6g ^{2}G – 4f ^{2}F^o													
λ5342.40	M17.06	1.65	$3.02^{(2.4)}_{(2.4)}$	0.10		1.27	$2.32^{(4.9)}_{(4.9)}$			4.49	$2.74^{(3.3)}_{(3.3)}$	0.31	2.98
M17.06 7g ^{2}G – 4f ^{2}F^o													
Average			**2.66 (6.9)**		**1.55**		**2.53 (5.8)**		**1.62**		**3.34 (4.1)**		**3.29**

[a] Liu et al. (2000), observations of the entire nebula.

[b] Liu et al. (2001).

[c] Liu et al. (2006), 2 arcsec wide-slit spectroscopy.

[*] Values in parentheses are the propagated uncertainties based on observational error (in per cent). The super- and subscripts are the errors added to and subtracted from the observed fluxes, respectively, and then corrected for extinction.

O and Ne ions and are mostly excited by recombination. The most numerous ionic species of C, N, O and Ne in the three PNe are in the doubly ionized stage, and the recombination lines emitted by them are prominent. Accurate measurements of these recombination lines allow us to derive reliable ionic abundances of the heavy elements. Setting $I(\lambda)$ as the observed intensity of a recombination line with wavelength λ emitted by an ion X^i, we derive the ionic abundance X^{i+1}/H^+ (i.e., the recombining ion) using

$$\frac{X^{i+1}}{H^+} = \frac{\lambda}{4861}\frac{\alpha_{\rm eff}(H\beta)}{\alpha_{\rm eff}(\lambda)}\frac{I(\lambda)}{I(H\beta)}, \quad (2)$$

where $\alpha_{\rm eff}(\lambda)$ and $\alpha_{\rm eff}(H\beta)$ are the effective recombination coefficients for λ and Hβ, respectively. The $\alpha_{\rm eff}(\lambda)/\alpha_{\rm eff}(H\beta)$ coefficient ratio is insensitive to the electron temperature and almost independent of the density. Here the effective recombination coefficients of helium and the heavy element ions, $\alpha_{\rm eff}(\lambda)$, were adopted from the literature, and $\alpha_{\rm eff}(H\beta)$ was adopted from Storey & Hummer (1995). Calculations and discussion of the ORL ionic abundances are presented below.

6.2.1 He^+/H^+ and He^{2+}/H^+

In this section, we derived the He^+/H^+ ionic abundances using the theoretical emissivities of Porter et al. (2012), using the best observed He I lines, λ4471, λ5786 and λ6678. The electron temperature diagnosed from the He I λ7281/λ6678 line ratio was assumed in the abundance calculations. The He^{2+}/H^+ ionic abundance ratio was derived using the He II λ4686 line, and the hydrogenic effective recombination coefficients of Storey & Hummer (1995) was adopted. The He^+/H^+ and He^{2+}/H^+ ionic abundance ratios derived for NGC 6153, M 1-42 and Hf 2-2 are presented in Table 6. The ionic and elemental abundances from the literature are also presented in Table 6 for comparison. For NGC 6153 and M 1-42, our He^+/H^+ abundance ratios generally agree with the literature, while for Hf 2-2, our abundance value is higher than that given by Liu et al. (2006). Difference in the He^{2+}/H^+ ratios is very small due to its low abundance compared with He^+.

There are about 40 He I emission lines identified in our spectra. While these lines mainly arise from recombination, the emissivities of some the He I lines may be contributed by collisional excitation and/or affected by self-absorption (e.g., Benjamin, Skillman & Smits 2002). In general the singlet lines are affected by Cases A or B, while the triplet lines are not. However, triplet lines could be affected by self-absorption from the 2s ^{3}S meta-stable state. Because of the large number of singlet lines detected with good signal-to-noise ratios, we have decided to derive the He^+/H^+ ratio making use of these lines. The He I lines detected in the UVES spectra are little affected by line blending. Thus both singlet and triplet lines can be used to derive He^+/H^+. We used the average He^+/H^+ ratio from the best detected He I lines (Table 6).

6.2.2 C^{2+}/H^+

Most of the C II optical recombination lines observed in our UVES spectra are excited by recombination, and a few are probably dominated by dielectronic recombination. Processes of dielectronic recombination, capture and radiative cascade, and radiative recombination of the C^+ ion are described in Fang & Liu (2013, Fig. 10 therein). A free electron with energies equivalent to the energy of a Rydberg state of C II can be captured and then cascade to the ground levels, emitting a series of lines. The captured electron on an autoionizing state can also return to a continuum level through autoionization and thus leaves an ion (i.e., the recombining ion) in

Table 8. Recombination line N^{2+}/H^+ abundances for NGC 6153, M 1-42 and Hf 2-2. Intensities are normalized such that Hβ = 100. The N II effective recombination coefficients were adopted from Fang, Storey & Liu (2013).

Line (Å)	Mult.	NGC 6153				M 1-42				Hf 2-2			
		20 minutes		Literature[a]		30 minutes		Literature[b]		30 minutes		Literature[c]	
		$\frac{I_{obs}}{I(H\beta)}$	N^{2+}/H^{+*} ($\times10^{-3}$)	$\frac{I_{obs}}{I(H\beta)}$	N^{2+}/H^{+} ($\times10^{-3}$)	$\frac{I_{obs}}{I(H\beta)}$	N^{2+}/H^{+*} ($\times10^{-3}$)	$\frac{I_{obs}}{I(H\beta)}$	N^{2+}/H^{+} ($\times10^{-3}$)	$\frac{I_{obs}}{I(H\beta)}$	N^{2+}/H^{+*} ($\times10^{-3}$)	$\frac{I_{obs}}{I(H\beta)}$	N^{2+}/H^{+} ($\times10^{-3}$)
3–3 transitions													
λ5666.63	M3	1.45	$1.57^{(2.5)}_{(1.9)}$	0.22	1.68	1.89	$5.14^{(1.4)}_{(1.4)}$	0.67	5.67	4.97	$2.70^{(7.0)}_{(7.0)}$	0.58	2.48
λ5676.02	M3	1.23	$2.88^{(2.8)}_{(3.1)}$	0.13	2.17	1.40	$6.57^{(1.8)}_{(1.8)}$	0.32	6.06	4.53	$2.66^{(3.0)}_{(3.8)}$	0.27	2.60
λ5679.56	M3	2.61	$1.62^{(1.9)}_{(1.9)}$	0.43	1.78	3.18	$5.93^{(5.0)}_{(5.0)}$	1.27	5.77	6.58	$2.04^{(5.0)}_{(5.0)}$	1.05	2.41
λ5686.21	M3	1.55	$2.04^{(3.9)}_{(3.9)}$	0.09	2.09	1.43	$5.66^{(1.6)}_{(1.4)}$	0.20	5.20	4.33	$3.42^{(12.6)}_{(13.2)}$	0.26	3.34
λ5710.77	M3	1.32	$2.00^{(2.5)}_{(3.0)}$	0.06	1.97	1.57	$7.14^{(3.1)}_{(3.1)}$	0.20	7.53	3.67	$4.45^{(2.2)}_{(2.2)}$	0.24	4.64
M3 3p ^{3}D – 3s ^{3}P°			**2.02 (2.3)**		**1.94**		**6.09 (11.5)**		**6.05**		**3.05 (2.7)**		**3.09**
λ4630.54	M5	1.28	$1.57^{(8.0)}_{(8.1)}$	0.21	1.78	1.04	$3.83^{(1.6)}_{(1.6)}$	0.44	3.91	2.46	$2.01^{(6.0)}_{(4.0)}$	0.46	2.17
M5 3p ^{3}P – 3s ^{3}P°													
λ3994.99	M12	1.50	$3.19^{(9.1)}_{(9.1)}$			0.66	$2.10^{(2.4)}_{(2.9)}$			2.32	$3.70^{(3.0)}_{(5.0)}$		
M12 3p ^{1}D – 3s ^{1}P°													
λ4803.29	M20	1.00	$1.76^{(6.0)}_{(11.0)}$	0.10	1.50	0.70	$3.69^{(3.8)}_{(4.1)}$			2.13	$2.50^{(4.0)}_{(5.0)}$		
M20 3p ^{3}D° – 3s ^{3}D													
Average			**2.17 (3.3)**		**1.64**		**3.20 (2.5)**		**3.91**		**2.74 (2.6)**		**2.17**
4f–3d transitions													
λ4035.08	M39a	1.52	$1.30^{(8.5)}_{(9.2)}$	0.09	1.04	0.71	$2.43^{(2.9)}_{(2.5)}$	0.30	2.38	2.58	$2.93^{(6.5)}_{(6.5)}$	0.53	3.19
λ4043.53	M39a	1.59	$1.45^{(7.6)}_{(8.6)}$	0.15	1.30	0.79	$2.86^{(1.4)}_{(1.4)}$	0.68	3.36	2.79	$2.54^{(7.9)}_{(8.7)}$	0.49	2.11
Average			**1.38 (5.5)**		**1.29**		**2.64 (8.1)**		**2.49**		**2.69 (3.9)**		**2.69**

[a] Liu et al. (2000), observations of the entire nebula.

[b] Liu et al. (2001).

[c] Liu et al. (2006), 2 arcsec wide-slit spectroscopy.

* Values in parentheses are the propagated uncertainties based on observational error (in per cent). The super- and subscripts are the errors added to and subtracted from the observed fluxes, respectively, and then corrected for extinction.

its ground state. In the physical conditions of PNe, autoionization usually dominates and the population of autoionizing states can be defined by the Saha and Boltzmann equations (i.e., the local thermodynamical equilibrium – LTE). The emissivity of a dielectronic recombination line is proportional to $\exp -E/kT_e$ (E is the excitation energy of this line). The intensity ratio of a dielectronic recombination line and a line excited by pure radiative recombination, can used to derive the electron temperature (Fang & Liu 2013).

We have detected nearly a dozen C II lines. These lines come from the multiplets M3 and M6 as well as some ng–4f transitions. The best observed (and thus accurately measured) multiplets of C II in our spectra are M3 λ7235 (3d ^{2}D – 3p ^{2}P°), M6 λ4267 (4f ^{2}F° – 3d ^{2}D) and some transitions belonging to the ng–4f ($n \geqslant 5$) array. For these transitions, we have used effective recombination coefficients from Davey, Storey & Kisielius (2000), whose calculations have only accounted for one electron density case at 10^4 cm^{-3}. They took great care in the relatively low temperatures ($T_e < 5000$ K). These calculations were under the *LS*-coupling assumption and only for the transitions that come from the ^{1}S state of the recombining ion C^{2+}.

In the abundance calculations of C^{2+}/H^+, an electron temperature of 1000 K, as derived from the N II and O II ORL ratios (Section 5.5; Figs 9–12), was assumed. We assumed that transitions between the doublet states of C II were in Case B, given that the ground state (^{2}P°) of C^+ is a doublet. The C^{2+}/H^+ abundance ratios derived from the best observed lines are presented in Table 7 for NGC 6153, M 1-42 and Hf 2-2. The adopted C^{2+}/H^+ abundance ratios in the current work are averaged from the abundances derived from individual lines. These values are also compared with those given in the literature. A review discussion of the current status of abundance determinations using the C II ORLs is given by Fang & Liu (2013).

6.2.3 N^{2+}/H^+

Figs 41 and 42 in Fang, Storey & Liu (2013) show the N^{2+}/H^+ and O^{2+}/H^+ abundance ratios calculated from the observed fine-structure lines belonging to different multiplets of the 3–3 transitions as well as the 4f–3d transition array. The N^{2+}/H^+ abundance ratios derived using the old version of the N II effective recombination coefficients (i.e., the *LS*-coupling calculations of Kisielius & Storey 2002) were also presented in Fang & Liu (2013) for purpose of comparison. They found that the ionic abundances derived from the 3–3 transitions generally consistent with those derived from the 4f–3d transitions of N II, when the new effective recombination coefficients of Fang, Storey & Liu (2013) were used.

Several dozen N II lines were identified in the spectra (Table 13). The M3 multiplet is the strongest transition of N II in the optical. Located in the blue region of our spectra (<4500 Å), the

Table 9. Recombination line O^{2+}/H^+ abundances for NGC 6153, M 1-42 and Hf 2-2. Intensities are normalized such that Hβ = 100. The O II effective recombination coefficients used for the abundance calculations were adopted from the unpublished calculations P. J. Storey.

Line (Å)	Mult.	NGC 6153				M 1-42				Hf 2-2			
		20 minutes		Literature[a]		30 minutes		Literature[b]		30 minutes		Literature[c]	
		$\frac{I_{obs}}{I(H\beta)}$	O^{2+}/H^{+*} ($\times10^{-3}$)	$\frac{I_{obs}}{I(H\beta)}$	O^{2+}/H^{+} ($\times10^{-3}$)	$\frac{I_{obs}}{I(H\beta)}$	O^{2+}/H^{+*} ($\times10^{-3}$)	$\frac{I_{obs}}{I(H\beta)}$	O^{2+}/H^{+} ($\times10^{-3}$)	$\frac{I_{obs}}{I(H\beta)}$	O^{2+}/H^{+*} ($\times10^{-3}$)	$\frac{I_{obs}}{I(H\beta)}$	O^{2+}/H^{+} ($\times10^{-3}$)
							3–3 transitions						
λ4638.86	M1	1.61	$5.22^{(2.5)}_{(7.0)}$	0.54	5.16	1.16	$6.57^{(1.7)}_{(8.3)}$	0.69	6.79	3.02	$0.92^{(6.8)}_{(7.0)}$	1.05	9.38
λ4641.81	M1	6.88	$3.92^{(2.3)}_{(7.2)}$	0.86	3.29	4.46	$3.81^{(1.8)}_{(1.5)}$	1.15	4.45	2.09	$7.13^{(7.1)}_{(7.1)}$	2.20	7.77
λ4649.13	M1	2.83	$2.35^{(3.0)}_{(1.7)}$	1.37	2.76	2.93	$3.91^{(5.0)}_{(2.6)}$	1.76	3.60	7.02	$5.20^{(3.8)}_{(3.2)}$	2.75	5.11
λ4650.84	M1	1.56	$3.08^{(3.6)}_{(5.1)}$	0.33	3.19							1.26	11.20
λ4661.63	M1	1.72	$3.33^{(1.8)}_{(4.9)}$	0.43	3.24	1.37	$4.98^{(1.2)}_{(7.3)}$	0.62	4.76	3.37	$7.82^{(5.7)}_{(5.7)}$	1.06	7.41
λ4673.73	M1	1.11	$3.75^{(6.7)}_{(7.3)}$	0.08	3.93	0.61	$3.42^{(5.3)}_{(8.3)}$			2.13	$3.61^{(4.1)}_{(4.1)}$		
λ4676.24	M1	1.43	$2.34^{(2.1)}_{(4.0)}$	0.30	2.69	1.07	$4.21^{(1.7)}_{(7.5)}$	0.44	3.99	2.67	$3.28^{(1.9)}_{(1.8)}$	0.43	3.58
λ4696.35	M1	0.96	$5.25^{(8.0)}_{(8.3)}$	0.06	5.02			0.07	5.53	1.79	$6.90^{(7.4}_{(7.4)}$		
M1 3p ^{4}D° – 3s ^{4}P			**3.65 (2.9)**		**3.53**		**4.48 (2.3)**		**4.85**		**4.98 (4.7)**		**7.41**
λ4317.14	M2	1.33	$2.06^{(6.3)}_{(4.0)}$	0.13	1.72	0.85	$3.28^{(2.1)}_{(7.5)}$	0.23	3.09	2.57	$3.33^{(1.6)}_{(3.0)}$	0.59	
λ4319.63	M2	1.47	$2.01^{(4.0)}_{(3.0)}$	0.16	1.95	0.64	$2.88^{(1.4)}_{(7.8)}$	0.21	3.09	2.62	$3.58^{(2.7)}_{(2.7)}$	0.27	
λ4325.76	M2	1.38	$5.44^{(16.2)}_{(7.9)}$	0.08	5.23	0.44	$2.46^{(8.9)}_{(8.4)}$	0.04	2.39	2.36	$3.10^{(2.4)}_{(2.4)}$		
λ4336.86	M2	1.21	$2.27^{(14.5)}_{(5.5)}$			0.74	$3.47^{(3.0)}_{(7.9)}$			1.89	$3.56^{(4.7)}_{(4.7)}$		
λ4345.56	M2	1.60	$3.79^{(7.1)}_{(6.1)}$	0.26	3.40			0.44	5.60			0.79	8.91
λ4349.43	M2	1.59	$2.63^{(2.7)}_{(4.1)}$	0.41	2.18	1.10	$2.74^{(11.0)}_{(6.1)}$	0.56	2.95	2.77	$3.46^{(1.6)}_{(2,4)}$	0.65	3.13
λ4366.89	M2	1.39	$2.58^{(3.1)}_{(4.8)}$	0.22	2.69	0.88	$4.34^{(12.0)}_{(8.0)}$	0.36	4.47	2.50	$5.30^{(5.3)}_{(5.3)}$	0.48	5.01
M2 3p ^{4}P° – 3s ^{4}P			**2.97 (3.9)**		**2.86**		**3.20 (19.1)**		**3.14**		**3.72(19.5)**		**5.68**
λ4414.90	M5	0.81	$4.18^{(4.1)}_{()}$	0.18	3.60	0.69	$3.56^{(1.0)}_{()}$	0.22	5.37	1.75	$9.06^{(11.5)}_{()}$	0.27	7.44
M5 3p ^{2}D° – 3s ^{2}P													
λ3973.26	M6	1.50	$4.92^{(13.2)}_{(7.4)}$			0.62	$10.25^{(5.0)}_{(9.4)}$			2.21	$10.35^{(7.9)}_{(7.9)}$		
M6 3p ^{2}P° – 3s ^{2}P													
λ4072.16	M10	2.70	$4.66^{(2.8)}_{(4.4)}$	1.02	4.25	2.23	$5.76^{(12.0)}_{(6.2)}$	1.30	5.24	4.07	$7.01^{(4.0)}_{(4.4)}$	2.05	7.43
λ4078.84	M10	1.30	$4.77^{(5.2)}_{(7.4)}$	0.17	4.75	0.68	$4.98^{(2.0)}_{(8.7)}$	0.22	5.71	2.25	$11.05^{(8.0)}_{(8.0)}$	0.45	10.70
λ4085.11	M10	1.41	$4.99^{(4.0)}_{(7.3)}$	0.21	4.74	0.83	$4.69^{(13.0)}_{(8.3)}$	0.23	4.93	2.34	$8.30^{(7.0)}_{(7.3)}$	0.42	8.14
λ4092.93	M10	1.41	$5.98^{(6.5)}_{(7.8)}$	0.18	5.60	0.64	$5.42^{(2.2)}_{(8.8)}$	0.20	5.90	2.29	$5.83^{(5.9)}_{(6.3)}$		
M10 3d ^{4}F – 3p ^{4}D°			**2.93 (12.9)**		**4.84**		**5.78 (3.7)**		**5.43**		**8.60(10.1)**		**8.43**
λ4132.80	M19	1.51	$2.44^{(7.4)}_{(4.3)}$	0.11	2.02	0.76	$4.91^{(1.8)}_{(8.5)}$	0.23	4.03	2.63	$9.66^{(7.1)}_{(7.5)}$	0.61	9.24
λ4153.30	M19	1.64	$3.00^{(4.0)}_{(4.8)}$	0.29	3.69	0.94	$4.33^{(12.0)}_{(7.9)}$	0.41	4.99	2.98	$8.74^{(6.4)}_{(6.8)}$	0.80	8.48
λ4169.22	M19	1.44	$3.36^{(6.0)}_{(6.0)}$	0.10	3.64	0.73	$4.54^{(4.6)}_{(8.5)}$	0.15	4.29	2.62	$12.23^{(7.9)}_{(7.9)}$	0.33	10.36
M19 3d ^{4}P – 3p ^{4}P°			**4.16 (3.5)**		**3.12**		**4.59 (5.2)**		**4.44**		**10.21 (14.5)**		**9.34**
Average			**3.62 (22.2)**		**3.59**		**4.67 (18.8)**		**4.46**		**6.88 (19.1)**		**7.71**
							4f–3d transitions						
λ4089.29	M48a	2.22	$4.45^{(2.5)}_{(5.1)}$	0.54	4.80	1.34	$5.37^{(9.0)}_{(7.5)}$	0.80	5.76	3.54	$5.90^{(3.9)}_{(4.2)}$	1.01	5.10
M48a 4f G[5]°–3d ^{4}F													
λ4083.90	M48b	1.39	$6.15^{(15.1)}_{(8.1)}$	0.20	6.05	0.81	$7.13^{(3.9)}_{(8.9)}$	0.30	7.54	2.19	$7.76^{(6.7)}_{(7.7)}$	0.45	7.82
M48b 4f G[4]°–3d ^{4}F													
Average			**5.30 (16.0)**		**5.42**		**6.25 (14.1)**		**5.92**		**6.83 (13.6)**		**6.46**

[a] Liu et al. (2000), observations of the entire nebula.

[b] Liu et al. (2001).

[c] Liu et al. (2006), 2 arcsec wide-slit spectroscopy.

[*] Values in parentheses are the propagated uncertainties based on observational error (in per cent). The super- and subscripts are the errors added to and subtracted from the observed fluxes, respectively, and then corrected for extinction.

Table 10. Recombination line Ne^{2+}/H^+ abundances for NGC 6153, M 1-42 and Hf 2-2. Intensities are normalized such that Hβ = 100. The effective recombination coefficients of the 3–3 transitions of Ne II were adopted from Kisielius et al. (1998), while the coefficient data of the 4f–3d lines were from the unpublished calculations of P. J. Storey.

Line (Å)	Mult.	NGC 6153				M 1-42				Hf 2-2			
		20 minutes		Literature[a]		30 minutes		Literature[b]		30 minutes		Literature[c]	
		$\frac{I_{obs}}{I(H\beta)}$	Ne^{2+}/H^{+*} ($\times10^{-3}$)	$\frac{I_{obs}}{I(H\beta)}$	Ne^{2+}/H^+ ($\times10^{-3}$)	$\frac{I_{obs}}{I(H\beta)}$	Ne^{2+}/H^{+*} ($\times10^{-3}$)	$\frac{I_{obs}}{I(H\beta)}$	Ne^{2+}/H^+ ($\times10^{-3}$)	$\frac{I_{obs}}{I(H\beta)}$	Ne^{2+}/H^{+*} ($\times10^{-3}$)	$\frac{I_{obs}}{I(H\beta)}$	Ne^{2+}/H^+ ($\times10^{-3}$)
						3–3 transitions							
λ3694.21	M1	3.17	$0.84^{(2.9)}_{(2.9)}$	0.45	1.36	1.00	$1.31^{(1.4)}_{(1.4)}$	0.45	1.39	5.97	$1.58^{(6.0)}_{(6.1)}$		
λ3709.62	M1	2.91	$1.29^{(11.5)}_{(11.6)}$	0.15	1.16	0.90	$1.59^{(12.1)}_{(12.2)}$			6.18	$1.09^{(4.7)}_{(4.8)}$		
M1 3p ^{4}D – 3s ^{4}P^o			**1.12 (15.7)**		**1.26**		**1.45 (9.7)**		**1.39**		**1.34 (18.4)**		
λ3334.84	M2	3.23	$0.99^{(4.3)}_{(4.3)}$	0.73	1.10	1.99	$1.83^{(2.1)}_{(2.1)}$	1.15	1.67	4.96	$1.52^{(9.6)}_{(9.9)}$		
λ3355.02	M2	3.37	$0.99^{(3.4)}_{(3.4)}$	0.46	1.31	1.77	$1.56^{(7.2)}_{(7.2)}$	0.82	1.84	5.68	$1.67^{(4.1)}_{(4.2)}$		
M2 3p ^{4}P – 3p ^{4}D^o			**0.99**		**1.20**		**1.70 (8.0)**		**1.76**		**1.60 (4.7)**		
λ3218.19	M13	4.00	$1.65^{(8.7)}_{(8.7)}$	0.50	1.20					7.24	$1.49^{(13.4)}_{(13.7)}$		
M13 3p ^{4}D^o – 3d ^{4}F													
Average			**1.17 (22.9)**		**1.22**		**1.57 (11.7)**		**1.57**		**1.47 (13.6)**		
						4f–3d transitions[d]							
λ4391.99	M55e	1.46	$1.27^{(4.8)}_{(4.9)}$	0.14	1.43	0.74	$1.71^{(2.8)}_{(2.7)}$	0.18	1.85	2.36	$2.05^{(5.5)}_{(5.9)}$	0.21	2.28
λ4409.30	M55e	1.36	$2.41^{(5.4)}_{(5.4)}$	0.13	2.07	0.57	$2.01^{(3.9)}_{4.0)}$	0.16	2.43	2.39	$2.54^{(8.8)}_{(9.2)}$		
M55 4f 2[5]^o – 3d ^{4}F			**1.84 (3.1)**		**1.75**		**1.86 (8.1)**		**2.14**		**2.30 (10.7)**		
λ4379.55	M60b	2.36	$2.35^{(3.0)}_{(3.0)}$			2.24	$0.90^{(1.2)}_{(1.2)}$	0.33	0.99	2.77	$0.69^{(6.9)}_{(7.1)}$		
M60b 4f 1[4]^o – 3d ^{2}F													
λ4428.64	M60c	1.13	$3.00^{(7.7)}_{(7.9)}$	0.10	2.41					1.77	$1.41^{(10.5)}_{(10.8)}$		
M60c 4f 1[3]^o – 3d ^{2}F													
λ4430.94	M61a	1.07	$2.63^{(4.7)}_{(3.7)}$	0.06	2.16					2.00	$2.46^{(14.0)}_{(15.0)}$		
M61a 4f 2[4]^o – 3d ^{2}D													
λ4457.05	M61d	1.22	$4.28^{(2.5)}_{(2.5)}$	0.05	5.15								
M61d 4f 2[2]^o – 3d ^{2}D													
λ4413.22	M65	096	$3.49^{(20.6)}_{(2.08)}$	0.07	2.90	0.64	$4.65^{(9.1)}_{(9.2)}$	0.11	4.63				
M65 4f 0[3]^o – 3d ^{4}P													
Average			**3.15 (2.2)**		**3.16**		**2.32 (6.1)**		**3.16**		**1.83 (3.8)**		**2.28**

[a] Liu et al. (2000), observations of the entire nebula.

[b] Liu et al. (2001).

[c] Liu et al. (2006), 2 arcsec wide-slit spectroscopy.

[*] Values in parentheses are the propagated uncertainties based on observational error (in per cent). The super- and subscripts are the errors added to and subtracted from the observed fluxes, respectively, and then corrected for extinction.

[d] Effective recombination coefficients are only available at one electron temperature and density case with T_e = 10,000 K and N_e = 10,000 cm^{-3}.

4f–3d lines of N II have three lines that are best observed. The best observed 3–3 transition lines of N II in our spectra are M3 (3d ^{3}D – 3p ^{3}P^o), M5 (3p ^{3}P – 3s ^{3}P^o), M12 (3p ^{1}D – 3s ^{1}P^o) and M20 (3p ^{3}D^o – 3s ^{3}D). The strongest transitions of the 4f–3d array include λ4035.08 (M39a 4f G[7/2]$_3$–3d ^{3}F$^o_2$), λ4041.31 (M39b 4f G[9/2]$_5$–3d ^{3}F$^o_4$), and λ4043.53 (M39a 4f G[7/2]$_4$–3d ^{3}F$^o_4$). Some of these N II lines have been adopted in plasma diagnostics (McNabb et al. 2013) for Galactic PNe. The effective recombination coefficients used in abundance calculations were adopted from Fang, Storey & Liu (2013).

It has been known that the N II triplet transitions among the 3s, 3p and 3d states, which are linked to the ground term 2p^2 ^{3}P resonance, can be excited by fluorescence excitation. Grandi (1976) has shown that resonance fluorescence by the He I λ508.64 (1s8p ^{1}P$^o_1$ – 1s^2 ^{1}S$_0$) line is a dominant mechanism to populate the 4s ^{3}P$^o_1$ level of N II in the Orion Nebula, and it should be responsible for the strengths of the M3 and M5 multiplets. By comparing the N^{2+}/H^+ abundance ratios derived from the 3–3 and 4f–3d transitions, this effect is probably insignificant in NGC 6153, M 1-42 and Hf 2-2. In the physical conditions of PNe, the 2p4f levels of N II are difficult to be enhanced by fluorescence (either by star light or by the resonance transitions) and they are only excited by radiative recombination. The ionic abundances derived from the 4f–3d transitions are expected to be more reliable. Grandi (1976) also suggests that Multiplets 28 and 20 could be excited by a combination of starlight and recombination. Abundances derived from best observed N II lines are presented in Table 8 for the three PNe. The adopted N^{2+}/H^+ abundance ratio in the current paper is listed as the average values. These values are also compared with those given in the literature.

Table 11. Total elemental abundances for NGC 6153, M 1-42 and Hf 2-2.

Element	log $N(X)/N(H)+12$														
	NGC 6153				M 1-42				Hf 2-2				Avg PN[a]		Solar[b]
	20 minutes		Literature[c]		30 minutes		Literature[d]		30 minutes		Literature[e]		Type 1	Type 2	
	ORL*	CEL*	ORL*	CEL*	ORL*	CEL*	ORL*	CEL*	ORL*	CEL*	ORL*	CEL*			
He	$11.12^{(4.0)}_{(4.1)}$		11.13		$11.16^{(2.2)}_{(2.2)}$		11.17		$11.07^{(4.3)}_{(4.5)}$		11.02		11.11	11.05	10.93
C	$9.46^{(9.0)}_{(10.0)}$		9.42	8.44	$9.40^{(3.0)}_{(5.7)}$		9.35	7.80	$9.62^{(9.2)}_{(3.1)}$		9.63		8.48	8.81	8.43
N	$9.36^{(12.7)}_{(13.5)}$	$8.20^{(3.4)}_{(2.4)}$	9.32	8.36	$9.84^{(7.6)}_{(7.6)}$	$8.77^{(2.8)}_{(1.7)}$	9.59	8.68	$9.54^{(18.7)}_{(20.7)}$	$8.00^{(11.0)}_{(10.7)}$	9.52	7.77	8.72	8.14	7.83
O	$9.51^{(14.2)}_{(16.6)}$	$8.51^{(10.9)}_{(11.1)}$	9.66	8.69	$9.56^{(8.4)}_{(3.9)}$	$8.75^{(14.4)}_{(13.7)}$	9.79	8.63	$9.72^{(13.1)}_{(13.6)}$	$8.35^{(14.1)}_{(16.2)}$	9.94	8.11	8.65	8.69	8.69
Ne	$9.21^{(5.5)}_{(4.9)}$	$8.18^{(17.1)}_{(22.5)}$	9.29	8.25	$9.31^{(5.4)}_{(4.8)}$	$8.12^{(11.3)}_{(10.1)}$	9.40	8.12	$9.33^{(5.3)}_{(4.9)}$	$7.87^{(13.2)}_{(13.4)}$	9.52	7.62	8.09	8.10	7.93
S		$7.00^{(4.1)}_{(4.1)}$		7.23		$6.90^{(7.5)}_{(2.4)}$		7.08		$6.69^{(11.4)}_{(3.4)}$		6.36	6.91	6.91	7.12
Cl		$5.77^{(9.2)}_{(4.6)}$		5.62		$5.52^{(5.2)}_{(10.8)}$		5.26		$5.64^{(14.2)}_{(11.9)}$					5.50
Ar		$6.20^{(9.0)}_{(3.0)}$		6.40		$6.10^{(2.8)}_{(2.1)}$		6.56		$5.78^{(18.1)}_{(12.3)}$		6.13			

[a] Kingsburg & Barlow (1994).

[b] Asplund et al. (2009).

[c] Liu et al. (2000), observations of the entire nebula.

[d] Liu et al. (2001).

[e] Liu et al. (2006), 2 arcsec wide-slit spectroscopy.

* Values in parentheses are the propagated uncertainties based on observational error (in per cent). The super- and subscripts are the errors added to and subtracted from the observed fluxes, respectively, and then corrected for extinction.

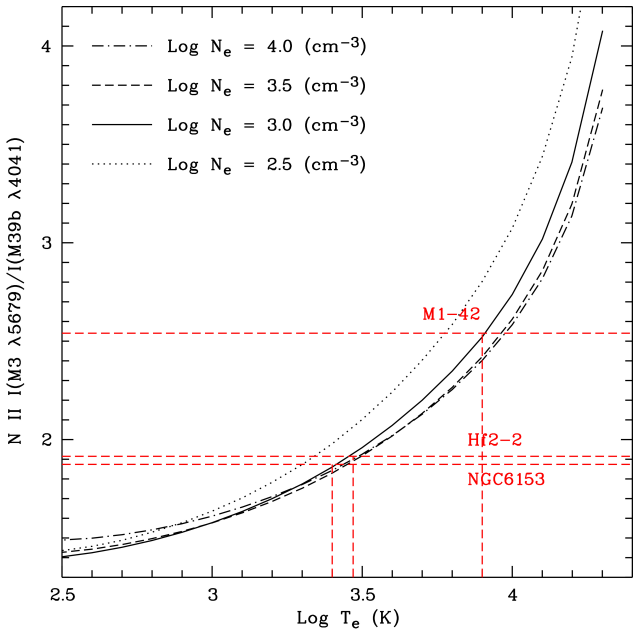

Figure 9. The N II λ5679/λ4041 intensity ratio as a function of the electron temperature. Different density cases are represented by different line types. The curves were created using the N II effective recombination coefficients of Fang, Storey & Liu (2011, 2013). The observed N II line ratios of NGC 6153, M 1-42 and Hf 2-2 were indicated by horizontal red dashed lines.

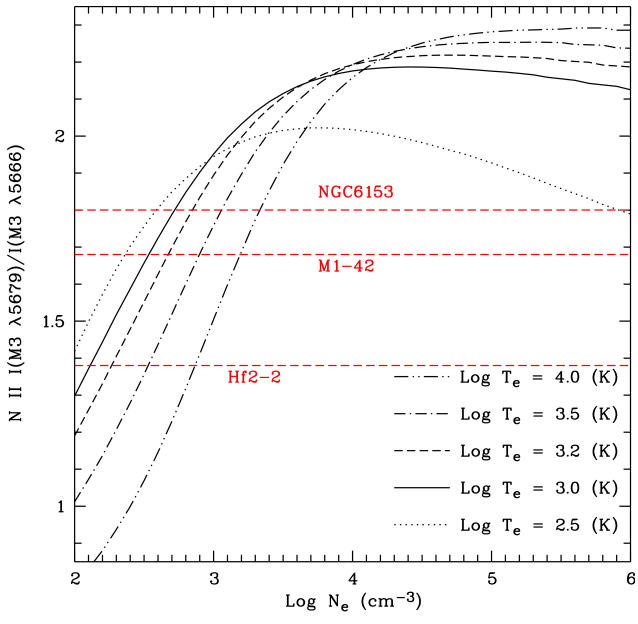

Figure 10. Same as Fig. 9 but for the N II λ5679/λ5666 intensity ratio as a function of the electron density. Different temperature cases are represented by different line types.

Fang & Liu (2013) provide a detailed review for deriving abundances using the N II ORLs.

6.2.4 O^{2+}/H^+

The O^{2+}/H^+ ionic abundances using the unpublished new effective recombination coefficients of P.J. Storey (private communication; see also Fang & Liu 2013). More than 80 emission lines of O II were detected in our spectra. The M1 $3p\,^4D^o - 3s\,^4P$ multiplet is the strongest among all O II transitions, and the ORLs of this multiplet is also the best observed (Fig. 3). The measurement uncertainties of the seven O II lines (λλ4638.86, 4641.81, 4649.13,

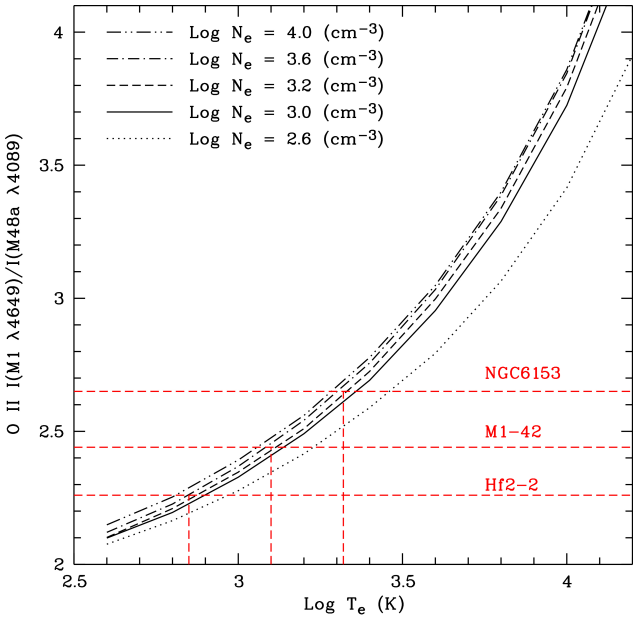

Figure 11. The O II λ4649/λ4089 intensity ratio as a function of the electron temperature. Different density cases are represented by different line types. The curves were created using the O II effective recombination coefficients of P. J. Storey (unpublished). The observed O II line ratios of NGC 6153, M 1-42 and Hf 2-2 were indicated by horizontal red dashed lines.

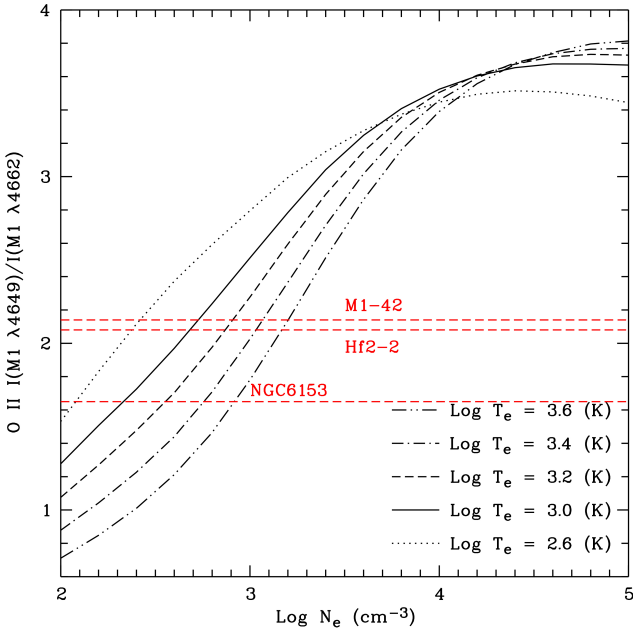

Figure 12. Same as Fig. 11 but for the O II λ4649/λ4662 intensity ratio as a function of the electron density. Different temperature cases are represented by different line types.

4650.84, 4661.63, 4673.73, 4676.24 and 4696.35) are all less than 10 per cent. In our abundance calculations, we did not consider the following lines: (1) lines with errors higher than 40 per cent, (2) lines affected by line blending, and (3) the O II λ4156.54 line of multiplet M19 because of possible line blending (Liu et al. 2000). An electron temperature of 1000 K (Section 5.5) was assumed in the abundance calculations of O^{2+}/H^+.

The O II optical recombination spectrum is prominent for all three PNe. The best observed 3–3 lines of O II belong to the multiplets M1 (3p ^{4}D^o – 3s ^{4}P), M2 (3p ^{4}P^o – 3s ^{4}P), M5 (^{2}D^o – 3s ^{2}P), M6 (3p ^{2}P^o – 3s ^{2}P), M10 (3d ^{4}F – 3p ^{4}D^o) and M19 (3d ^{4}P – 3p ^{4}P^o). The best observed multiplets of the 4f–3d transitions of O II include M48a (4f G[5]^o–3d ^{4}F) and M48b (4f G[4]^o–3d ^{4}F). These lines have also been adopted in plasma diagnostics for PNe and H II regions (McNabb et al. 2013). Abundances derived from the best observed lines are presented in Table 9, with the adopted O^{2+}/H^+ abundance ratio taken from the averaged M1 abundance in the current work. These values are also compared with those given in the literature. The adopted O^{2+}/H^+ abundances of the three PNe were averaged from the different transitions. Differences between our values and those in the literature can be explained by either the different instrumentation used or by the different analysis methodology implemented.

6.2.5 Ne^{2+}/H^+

We have detected about a dozen permitted lines of Ne II. In our abundance calculations of Ne^{2+}/H^+ from the the 3–3 transitions, we adopted the effective recombination coefficients of Kisielius et al. (1998), which were calculated in the *LS* coupling. Analytical fits, which are reliable in 2000–20 000 K, of the effective recombination coefficients as a function of the electron temperature were given in Kisielius et al. (1998). The Ne^{2+}/H^+ ionic abundances are presented in Table 10 for NGC 6153, M 1-42 and Hf 2-2. For For the 4f–3d transitions of Ne II, the effective recombination coefficients were adopted from the unpublished calculations of P.J. Storey (private communications). However, these coefficients are only available for the case where T_e = 10 000 K and N_e = 10^4 cm^{-3}. Difference between the Ne^{2+}/H^+ abundances derived from the 4f–3d transitions and those derived from the 3–3 transitions is noticeable. This is mainly due to the inadequacy of the current versions of the Ne II effective recombination coefficients (Fang & Liu 2013).

The Ne^{2+}/H^+ abundances adopted for the three PNe are averaged from the 4f–3d transitions whose measurements are reliable. Abundances derived from the best-detected lines are listed in Table 10 for NGC 6153, M 1-42 and Hf 2-2. The averaged N^{2+}/H^+ abundances are adopted for the three PNe. These values are also compared with those given in the literature. Fang, Storey & Liu (2013) provide a detailed review for deriving abundances using Ne II ORLs.

Other recombination lines, such as C III, N III and O III, could also be used as potential temperature diagnostics (Fang & Liu 2013). However, given their lack of adequate atomic data, these lines can not be adopted in plasma diagnostics now.

6.3 Ionic abundance discrepancies

Comparison of the ionic abundances of heavy elements derived from ORLs and CELs is presented in Fig. 13, where the ionic abundances of NGC 6153, M 1-42 and Hf 2-2 from the literature are also overploted. The ionic abundances derived from CELs are from Table 5, while the ORL abundances are from Tables 7–10. The O^{2+}/H^+ ionic abundances derived from ORLs are higher than the CELs values by a factor of $\sim$10 for NGC 6153, 25 for M 42, and 63 for Hf 2-2. These discrepancies (ADFs) are consistent with the previous observations for the three PNe (Liu et al. 2000, 2001, 2006).

Table 12. Abundance discrepancy factors.

Element	ADF					
	NGC 6153		M 1-42		Hf 2-2	
	20 minutes	Literature[a]	30 minutes	Literature[b]	30 minutes	Literature[c]
N	$11.41^{(16.0)}_{(15.9)}$		$22.44^{(10.5)}_{(9.3)}$		$83.46^{(5.2)}_{(3.1)}$	
O	$11.17^{(12.6)}_{(17.7)}$	9.00	$21.85^{(5.9)}_{(4.0)}$	22.00	$81.51^{(12.2)}_{(4.3)}$	84.00
Ne	$11.27^{(7.3)}_{(4.8)}$		$22.91^{(5.5)}_{(4.7)}$		$83.01^{(5.5)}_{(4.8)}$	

[a] Liu et al. (2000), observations of the entire nebula.

[b] Liu et al. (2001).

[c] Liu et al. (2006), 2 arcsec wide-slit spectroscopy.

* Values in parentheses are the propagated uncertainties based on observational error (in per cent). The super- and subscripts are the errors added to and subtracted from the observed fluxes, respectively, and then corrected for extinction.

The ADF value in the Ne^{2+}/H^+ ionic abundance is 12 for NGC 6153, 18 for M 1-42, and 40 for Hf 2-2, if we adopt the ionic abundances calculated from the 3–3 transitions of Ne II. The ADFs of the former two PNe agree well with the literature, but differs in the case of Hf 2-2. If we adopt the abundances calculated from the 4f–3d transitions of Ne II, the ADF(Ne^{2+}) will be ∼30 for NGC 6153, 27 for M 1-42 and ∼50 for Hf 2-2. The difference between our ADFs and those in the literature probably comes from the measurements of line fluxes.

It is also worth noting that the commonly used effective recombination coefficients for the 3–3 transitions of Ne II were calculated by Kisielius et al. (1998), which are no longer adequate for nebular analysis and need to be thoroughly revised (Fang & Liu 2013). The effective recombination coefficients for the 4f–3d lines of Ne II have so far only been calculated at T_e = 10 000 K and N_e = 10^4 cm^{-3} (P. J. Storey, private communications), and more temperature and density cases need to be considered. New quantum-mechanical calculations of the Ne II effective recombination coefficients are now in progress (X. Fang et al., in preparation). These calculations are in the intermediate-coupling scheme and will be extended to the electron temperatures well below 1000 K.

6.4 Elemental abundances

The elemental abundances derived from CELs and ORLs are presented in Table 11 for NGC 6153, M 1-42 and Hf 2-2. We adopted the classical ionization correction factor (ICF) method from Kingsburg & Barlow (1994), who derived empirical ICFs of PNe based on observations of more than 60 southern Galactic PNe. This method relies mainly on the similarity of ionization potentials between various ions. The Equations 3–10 were used to calculate total C, N, O and Ne abundances from the ionic abundances. The ADF values in N, O and Ne derived for the three PNe are presented in Table 12 along with the values from the literature.

$$\begin{aligned}\frac{\mathrm{O}}{\mathrm{H}} &= \mathrm{ICF(O)} \times \left(\frac{\mathrm{O^+}}{\mathrm{H^+}} + \frac{\mathrm{O^{2+}}}{\mathrm{H^+}}\right) \\ &= \left(\frac{\mathrm{He^+} + \mathrm{He^{2+}}}{\mathrm{He^+}}\right)^{2/3} \times \left(\frac{\mathrm{O^+}}{\mathrm{H^+}} + \frac{\mathrm{O^{2+}}}{\mathrm{H^+}}\right).\end{aligned} \quad (3)$$

This equation was used to derive the CEL elemental abundance of oxygen. The He^+/H^+ and He^{2+}/H^+ ionic abundances are given in Table 6. For the ORL abundance of oxygen, we assumed that recombination line O^+/O^{2+} number ratio is the same as that derived from the CELs. Given that the very small fraction of oxygen in O^+, the errors introduced by this assumption are expected to be negligible.

For the carbon abundance, we adopted the equation

$$\frac{\mathrm{C}}{\mathrm{H}} = \mathrm{ICF(C)} \times \frac{\mathrm{C^{2+}}}{\mathrm{H^+}} = \frac{\mathrm{O}}{\mathrm{O^{2+}}} \times \frac{\mathrm{C^{2+}}}{\mathrm{H^+}}. \quad (4)$$

For the neon abundance, we used the equation

$$\frac{\mathrm{Ne}}{\mathrm{H}} = \mathrm{ICF(Ne)} \times \frac{\mathrm{Ne^{2+}}}{\mathrm{H^+}} = \frac{\mathrm{O}}{\mathrm{O^{2+}}} \times \frac{\mathrm{Ne^{2+}}}{\mathrm{H^+}}. \quad (5)$$

For nitrogen, we use the equation

$$\frac{\mathrm{N}}{\mathrm{H}} = \mathrm{ICF(N)} \times \frac{\mathrm{N^{2+}}}{\mathrm{H^+}} = \frac{\mathrm{O^+}}{\mathrm{H^+}} \times \frac{\mathrm{N^{2+}}}{\mathrm{H^+}}. \quad (6)$$

The elemental abundance of sulfur was derived using the equation

$$\frac{\mathrm{S}}{\mathrm{H}} = \mathrm{ICF(S)} \times \left(\frac{\mathrm{S^+}}{\mathrm{H^+}} + \frac{\mathrm{S^{2+}}}{\mathrm{H^+}}\right), \quad (7)$$

where

$$\mathrm{ICF(S)} = \left[1 - \left(1 - \frac{\mathrm{O^+}}{\mathrm{O}}\right)^3\right]^{-1/3}. \quad (8)$$

For argon, three stages of ionization (Ar^{2+}, Ar^{3+} and Ar^{4+}) were observed, and its elemental abundance was calculated using the equation

$$\frac{\mathrm{Ar}}{\mathrm{H}} = \mathrm{ICF(Ar)} \times \left(\frac{\mathrm{Ar^{2+}}}{\mathrm{H^+}} + \frac{\mathrm{Ar^{3+}}}{\mathrm{H^+}} + \frac{\mathrm{Ar^{4+}}}{\mathrm{H^+}}\right), \quad (9)$$

where

$$\mathrm{ICF(Ar)} = \frac{1}{1 - \mathrm{N/N^+}}. \quad (10)$$

The faint [Ar V] lines were detected in the spectra of our PNe, but their measurements are of large uncertainty. However, the ionic concentration of Ar^{4+} is very low (and thus Ar^{4+}/H^+ abundance ratio is not presented in Table 5) compared to the Ar^{2+} and Ar^{3+} ions. The ICF of the chlorine abundance was not discussed in Kingsburg & Barlow (1994). We estimated the Cl/H abundance ratio based on the similarities of the ionization potentials of the Cl and S ions.

The elemental He/H abundances derived from the current analysis agree well with the average value of the bulge (11.05) and disc sample (11.05) (Wang & Liu 2007) as well as the Solar value (Asplund et al. 2009). The elemental N/H abundances derived from CELs for NGC 6153, M 1-42 and Hf 2-2 all agree well with the

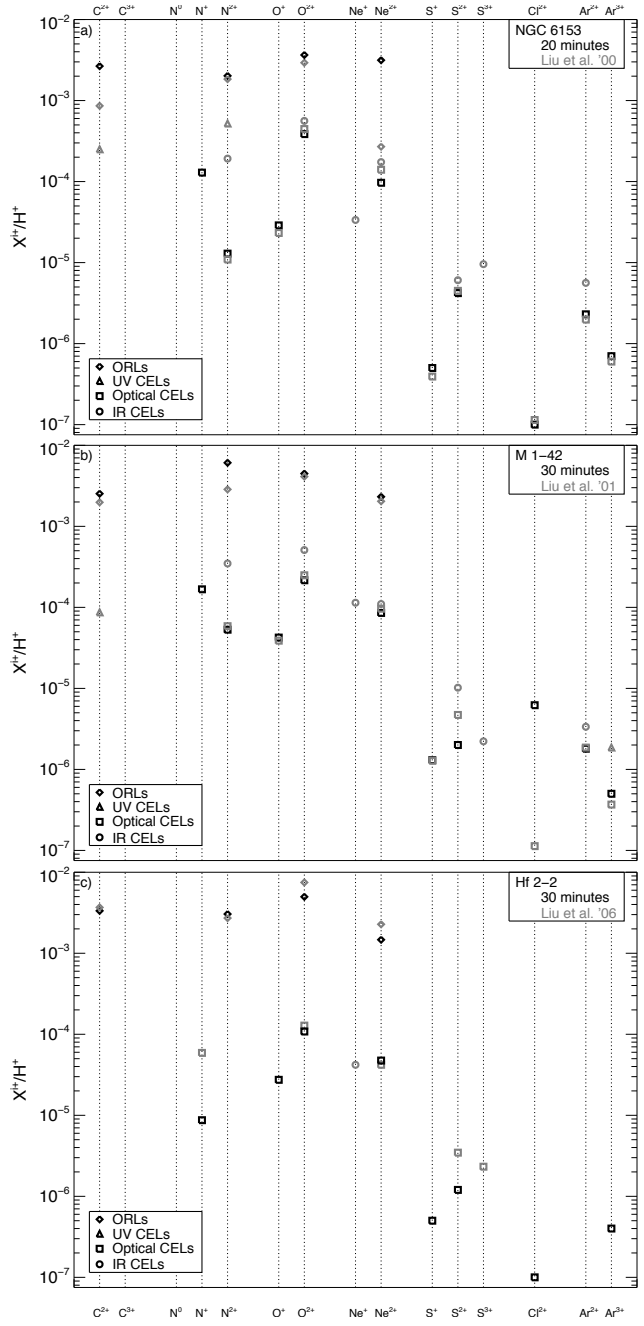

Figure 13. Comparison of the ionic abundances derived from ORLs and those from the UV, optical and IR CELs for NGC 6153 (top), M 1-42 (middle), and Hf 2-2 (bottom). Different symbols indicate different types of transitions. Data from the literature are presented for purpose of comparison: Liu et al. (2000)–Liu00, Liu et al. (2001)–Liu01, and Liu et al. (2006)–Liu06.

Solar value obtained by Asplund et al. (2009) as well as the average value of the bulge (8.61) and disc (9.05) samples compiled by Wang & Liu (2007). The elemental Ne/H abundances derived from CELs for the three PNe are all slightly above the Sun as well as the average bulge (8.05) and disc (8.09) values compiled by Wang & Liu (2007). The CEL O/H abundances derived for NGC 6153, M 1-42 and Hf 2-2 also agree well with the Solar value obtained by Asplund et al. (2009) as well as the average value of the bulge (8.72) and disc (8.71) samples compiled by Wang & Liu (2007).

Table 13. Number of permitted lines identified for all ionic species.

Ion	No. of lines		
	NGC 6153	M 1-42	Hf 2-2
	20 minutes	30 minutes	30 minutes
H I	61	37	55
He I	45	25	20
He II	29	17	10
C I	1		
C II	8	6	6
C III	5	4	2
N I	2		
N II	46	29	30
N III	15	11	7
O I	1		
O II	77	56	57
O III	26	18	3
Ne II	25	16	11
Mg I]	2	2	2
Si II	6	6	
Si III	1	2	1
Fe I	1		
Fe II	1		1

Table 14. Number of forbidden lines identified for all ionic species.

Ion	No. of lines		
	NGC 6153	M 1-42	Hf 2-2
	20 minutes	30 minutes	30 minutes
[C I]	2	1	1
[N II]	4	4	3
[O I]	2	2	
[O II]	3	3	3
[O III]	5	3	3
[Ne III]	4	4	4
[Ne IV]	1		1
[S II]	3	2	3
[S III]	3	3	3
[Cl II]	2	1	1
[Cl III]	3	2	2
[Cl IV]	2	2	1
[Ar III]	3	3	2
[Ar IV]	4	3	3
[Cr II]	1		
[Mn V]	1		
[Fe II]	2		
[Fe III]	2		1
[Fe IV]	2	1	1
[Ni II]	1		

The sulphur, chlorine and argon abundances of NGC 6153, M 1-42 and Hf 2-2 also agree well with the average abundance of the bulge and disc samples of Wang & Liu (2007) as well as the Solar values.

7 DISCUSSION

7.1 The Balmer jump fit

Our VLT UVES spectra of NGC 6153, M 1-42 and Hf 2-2 (Fig. A1) are very deep and of high spectral resolution. The line fluxes measured in the long-exposure spectra of NGC 6153, M 1-42 and Hf 2-2 are presented in Table 2 along with the measurement errors.

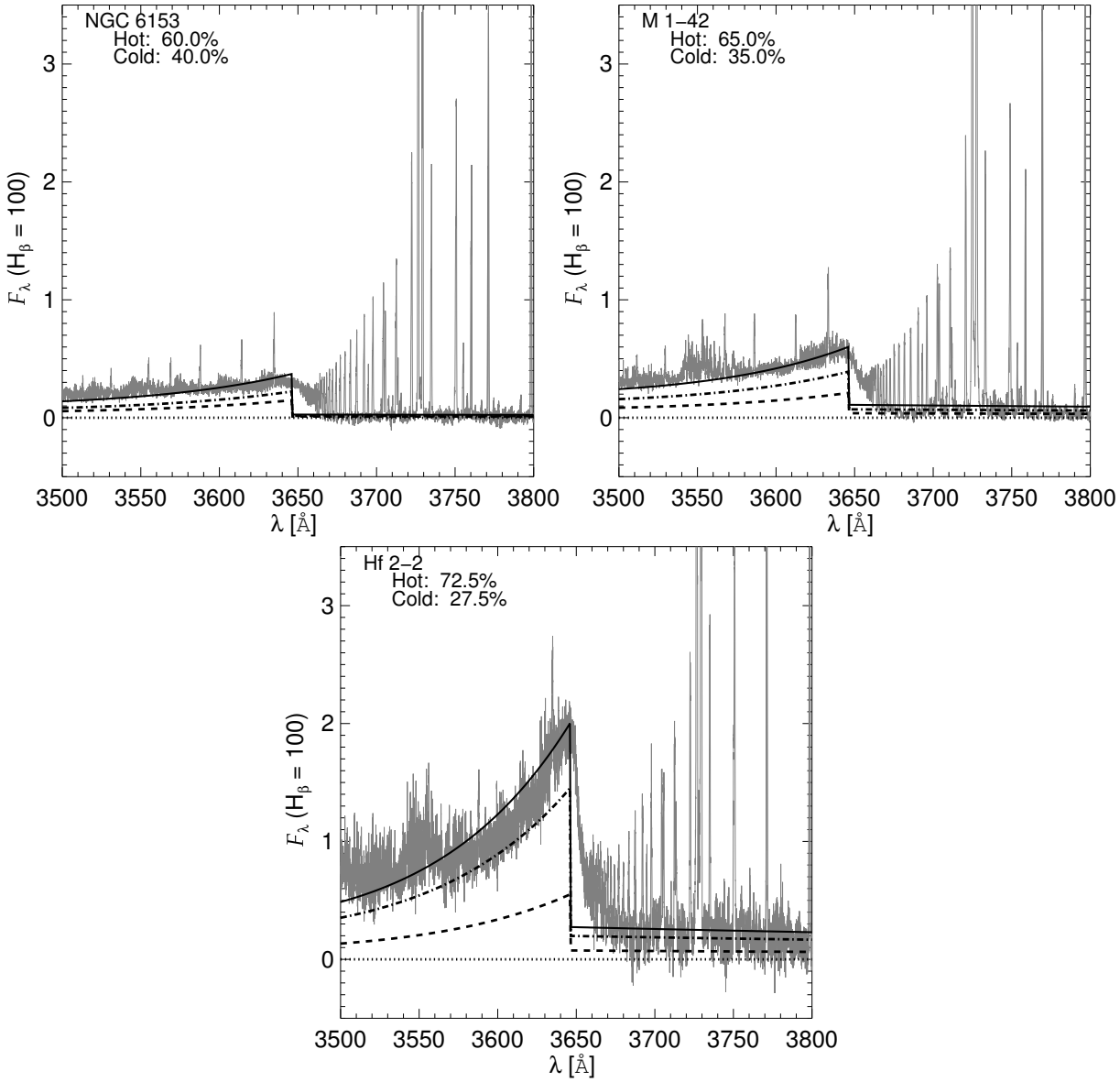

Figure 14. The echelle spectra (in grey color) of NGC 6153 (top-left panel), M 1-42 (top-right panel) and Hf 2-2 (bottom panel) showing the spectrum near the Balmer jump. The black solid curve is the two-component fit to the continuum using the method of Zhang, Liu & Zhang (2014). The continuum includes a very small contribution from the central star (the dotted line). The dot-dashed and dashed lines are the modeled spectrum of the hot (10^4 K) and cold (10^3 K) components, respectively. Contributions in percentage from the hot and cold components are presented in each panel. The spectra have not been corrected for extinction and are normalized such that $F(\mathrm{H}\beta) = 100$.

We tried to determine the percentage of the hot and cold emission components in the three PNe by fitting the hydrogen recombination continuum around the Balmer jump using two analytical formulae. The method of Zhang, Liu & Zhang (2014) was used in the fitting. Fig. 14 shows the continuum fitting around the Balmer jump for the long-exposure spectra of NGC 6153, M 1-42 and Hf 2-2. The fitting provides a rough estimate of how much ionized material comes from the cold (∼1000 K) and hot (∼10 000 K) plasma. Percentages of the emitting gas are presented in Fig. 14. Our analytical fits to the nebular continuum around the Balmer jump of the three PNe show that the majority of the observed continuum comes from the 10^4 K hot plasma (Fig. 14), indicating that a small amount of the cold component may account for the observed Balmer jump, which is generally consistent with the results of the Zhang, Liu & Zhang (2014). For Hf 2-2, more than 70 per cent of the continuum emission comes from the hot plasma, and less than 30 per cent is emitted by the cold component. Our continuum fits only provide a rough estimate, and more accurate fitting and comprehensive discussion are presented in Zhang, Liu & Zhang (2014).

7.2 Physical conditions

The density-sensitive CEL ratios [O II] λ3726/λ3729, [S II] λ6731/λ6716 and [Cl III] λ5537/λ5517 were used to derive the electron densities for the three PNe. The temperature-sensitive CEL ratios of [O III], [O II], [N II], [Ne III], [Ar III], [S II] and [S III] were used to derive the electron temperatures. The electron temperatures and densities were calculated using the EQUIB code. The temper-

atures derived from the [Ne III] ($\lambda3868 + \lambda3967$)/$\lambda3342$ nebular-to-auroral line ratio for NGC 6153, M 1-42 and Hf 2-2 were systematically higher than those derived from other diagnostic ratios. The [Ne III] temperature is probably unreliable due to two possible reasons: (1) The [Ne III] $\lambda\lambda3868,3967$ nebular lines are in a different order of the spectrum from the [Ne III] $\lambda3342$ auroral line, and errors might be introduced when we scaled the two orders of the spectrum to the same level and joined them together; (2) like the auroral lines of [N II], [O II] and [O III], whose fluxes could be partially contributed by the recombination process (Liu et al. 2000), the [Ne III] $\lambda3342$ auroral line might also be enhanced by the recombination process, which will lead to an overestimated electron temperature. Since our flux calibration is expected to be reliable, which can be inferred from the general consistency between the temperatures diagnosed from different CEL ratios (Table 4), the second reason might be the main cause of the relatively high temperature derived from the [Ne III] line ratio. However, detailed quantitative studies are needed to confirm this.

The electron densities are presented in Table 4. For all three PNe studied, intensity ratio of the [S II] $\lambda6716/\lambda6731$ doublet yields relatively lower electron densities than other diagnostic ratios. The [S II] densities might be problematic because the [S II] lines could be suppressed by collisional de-excitation, given that the critical densities[5] of the upper levels of $\lambda\lambda6716,6731$ are 1400 and 3600 cm^{-3}, respectively, which are comparable to the typical nebular densities. The same problem might happens to the [N I] nebular lines, whose intensity ratio also yields relatively low electron densities, compared with [O II], [Cl III], and [Ar IV]. The critical densities of the [N I] $\lambda\lambda5198,5200$ nebular lines are 1800 and 780 cm^{-3}, respectively. Therefore, the [N I] and [S II] densities are not included in density average.

As discussed in Section 5.2, the auroral lines of N II, O II and O III could be enhanced by recombination excitation(Liu et al. 2000). It turns out that the contribution of recombination to the auroral line intensities of [N II], [O II], and [O III] has very small effect on the derived electron temperatures, only reducing the temperatures by 1.55, 2.3 and 1.1 per cent for NGC 6153, M 1-42 and Hf 2-2, respectively. These corrections are also presented in Fig. 6. Conventionally, it is more appropriate to use the ionic abundances derived from the infrared forbidden lines instead of the recombination line abundances.

For the aforementioned cases, the CEL temperatures were adopted to derive the intensity contribution from the recombination process. This is suitable for a chemically homogeneous nebula. If there is 'cold', metal-rich component in the nebula, the recombination contribution to the auroral line fluxes of [N II], [O II] and [O III] may need to be considered. According to the previous discussion (see also Fang & Liu 2013), although the metal-rich component in PNe may contribute to the recombination enhancement of the auroral lines, the majority of the emission still comes from the hot plasma. Photoionization modeling is needed to estimate the relative contributions of these line fluxes from the two nebular components with largely different temperatures.

It is difficult to deduce a single electron density for the three PNe from the relative intensities of the high-n Balmer/Paschen lines (Figs 7 and 8) by simply using a least-squares optimization. Fig. 7 shows that the hydrogen Balmer lines with $n > 14$ have relatively high intensities that yield electron densities $\sim10^5$–10^6 cm^{-3}, while the lower-n Balmer lines yield electron densities around 10^4 cm^{-3}. Fig. 8 shows the same trend. Thus the electron densities deduced from the Balmer and Paschen decrements in Table 4 are only representative of the lower-n hydrogen lines. This density is higher than the CEL densities, indicating the condensation of ionized matter in these PNe, as suggested by Liu et al. (2000). By fitting simultaneously the observed continuum near the Balmer jump and the high-order Balmer emission lines, Zhang et al. (2004) derived an electron density of ~400 cm^{-3} for Hf 2-2, which is much lower than ours. Measurement errors of the Balmer lines are systematically smaller than those of the relatively weaker Paschen lines, and the low-order hydrogen lines generally have smaller errors than the high-n lines.

7.3 Possible origin of the abundance discrepancy

The 'cold', metal-rich inclusions proposed to exist in PNe generally well explain the observations (Liu 2006b). Our analyses of the UVES spectra of the three high-ADF PNe were carried out in a consistent manner: the recombination-line temperature ($\sim$1000 K) was assumed in the ORL abundance analysis, and the CEL temperature ($\sim$10 000 K) yielded was assumed in the forbidden-line abundance calculations. Prior to the availability of the high-quality effective recombination coefficients of the ORLs of heavy elements, Liu et al. (2000) adopted the [O III] temperature of 9100 K to calculate the recombination-line abundances of heavy elements in NGC 6153. In the abundance analyses of M 1-42, Liu et al. (2001) adopted the H I Balmer jump temperature (3560 K) to derive the ORL abundances. Given that these temperatures assumed were not based on the ORLs of heavy elements, the ORL abundances previously derived could be questionable (Fang & Liu 2013).

The ORLs of N II and O II probe the regions where the heavy element recombination lines are emitted. Thus the electron temperatures ($\sim$1000 K) derived from these ORL ratios reflect the physical conditions of these cold regions. Such a huge difference between the ORL and the CEL temperatures, together with the high ADFs observed in the three PNe (NGC 6153, ADF$\sim$10; M 1-42, ADF$\sim$20; Hf 2-2, ADF$\sim$70), can only be explained by the bi-abundance nebular model (e.g., Yuan et al. 2011), while temperature fluctuations and/or density inhomogeneities are difficult to interpret (Liu 2006b). A temperature sequence T_e(N II, O II ORLs) $\lesssim$ T_e(He I) $\lesssim$ T_e(H I) $\lesssim$ T_e(CELs), which is in line with what is predicted by the bi-abundance nebular model (Liu 2003; Péquignot, Liu & Barlow 2003), has been confirmed in our target PNe. All these lead to our conclusion that our assumption of bi-abundance model for the PNe is probably reasonable.

The 'cold', H-deficient plasma component in PNe is still not well understood and cannot be predicted by the current stellar evolution models. *Hubble Space Telescope* imaging reveals many [O III] line-emitting, H-deficient knots close to the central stars of a rare group of PNe including Abell 30 and Abell 78 (e.g., Borkowski et al. 1993; Borkowski, Harrington & Tsvetanov 1995). These knots are embedded in a round, limb-brightened faint nebula with angular diameter as large as 2 arcmin. These particular objects are identified as the 'born-again' PNe: PNe experience a final helium shell flash that brings the central star back to the AGB phase, subsequently repeating the PN evolution (Iben et al. 1983). Spectroscopic observations of the Abell 30 and Abell 58 reveal that emission from these H-deficient knots are dominated by ORLs of C, N, O and Ne, and the ADF values of the knots are as large as several hundred (Wesson, Liu & Barlow 2003; Wesson et al. 2008). Detailed 3D photoionization modeling of the H-deficient knots in Abell 30 confirms that the ORLs are emitted from the electron temperature as

[5] At an electron temperature of 10 000 K.

low as several hundred K (Ercolano et al. 2003). The above studies lead to the hypothesis that the 'born-again' event might be an explanation of the H-deficient inclusions in PNe. However, detailed ORL abundance analyses show that the knots in Abell 30 and Abell 58 are both O-rich, not C-rich as expected from the theory of the 'born-again' PNe Iben et al. (1983).

It is suggested that the abundance discrepancy may be related to the binary central stars of PNe, which is an intriguing topic as the central star of the extremely high-ADF PN Hf 2-22 (ADF$\sim$70; Liu et al. 2006) is a close binary system (Lutz et al. 1998). Spectroscopic observations of three high-ADF PNe (Abell 46, Abell 63 and Ou 5) with post common-envelope binary central stars seem to support the existence of the cold ($\sim10^3$ K), metal-rich ionized component (Corradi et al. 2015). The link between ADF and binarity of the central star has recently been further strengthened through studies of NGC 6778 (Jones et al. 2016), a PN with ADF$\sim$20. In spite of these efforts, detailed investigations are still needed to clarify whether the abundance discrepancy is physically related with binarity and how.

Another postulation is that the H-deficient inclusions in PNe might have their origins in the debris planetary systems of the progenitor stars (e.g., Liu 2003, 2006a). In the future, high spatial-resolution imaging and high-dispersion spectroscopic observations, with an aid of detailed 3D photoionization modeling, will help to understand the origin and evolution of the H-deficient plasma inclusions in PNe. Oxygen is not the only element that we found to have ADFs when comparing its abundances derived from both ORLs and CELs. Nitrogen and Neon are also relatively abundant heavy elements in both ORLs and CELs, and their ADF values are above unity, indicating they could also arise from the cold, H-deficient secondary component. We find that our results compare well with the previous literature. Table 12 lists the ADFs found for Nitrogen, Oxygen and Neon for all seven exposures of NGC 6153, M 1-42 and Hf 2-2.

7.4 Reliability of atomic data

Calculations of the He I recombination spectrum started as early as 1950s and continued to improve until recently (e.g., Mathis 1957; Brocklehurst 1972; Smits 1996; Benjamin, Skillman & Smits 1999, 2002; Bauman et al. 2005; Porter et al. 2005, 2012). Using the He I atomic model of Smits (1996) and the collisional data of Sawey & Berrington (1993), Benjamin, Skillman & Smits (1999) calculated the He I line emissivities. The data of Benjamin, Skillman & Smits (1999) has been adopted in plasma diagnostics for PNe and the results are consistent with what is expected from the bi-abundance nebular model (Zhang et al. 2005b). The more recent theoretical calculations of the He I line emissivities of (Porter et al. 2012) have incorporated ab initio photoionization cross-sections to the Case B collisional-recombination calculations of the He I spectrum.

The reliability of the effective recombination coefficients (i.e., the collision-recombination theory) of heavy element ions can be assessed by comparing ionic abundances derived from ORLs within a given multiplet, or from different multiplets. Liu et al. (1995, 2000, 2001) and Fang & Liu (2013) provide critical analyses of ORLs of the heavy elements, and show improvement in the new recombination coefficients when compared with the old atomic data.

The new calculations of the N II (Fang, Storey & Liu 2011, 2013) and O II (P. J. Storey, private communications) effective recombination coefficients are a great improvement over the previous work (e.g., Escalante & Victor 1990; Péquignot, Petitjean & Boisson 1991; Storey 1994; Kisielius & Storey 2002; Bastin & Storey 2006). Discussion of the reliability of these new effective recombination coefficients is presented in Liu (2012b). Fang & Liu (2013) critically analyzed the rich ORLs of the heavy elements observed in the very deep spectrum of NGC 7009. These new effective recombination coefficients were then utilized to construct diagnostic tools by McNabb et al. (2013), who carried out plasma diagnostics for more than 100 Galactic PNe, including NGC 6153, M 1-42 and Hf 2-2. The electron temperature and density of each nebula were derived simultaneously by locating the minimal difference between the observed and theoretical line intensities (McNabb et al. 2013, Sections 2.3 and 2.4 therein). The theoretical line intensities were derived from the new effective recombination coefficients of N II and O II.

7.5 Emission line numbers

Table 13 summarizes the numbers of permitted lines identified for different ionic species in the three PNe. In total, 353 permitted lines were identified for the long exposure (20 min) spectrum of NGC 6153 and 168 for the short-exposure (2 min) one with most of them excited mainly by recombination. For M 1-42, 229 permitted lines are identified for the long-exposure (30 min) spectrum, 205 for the medium-exposure (15 min) spectrum and 116 for the short-exposure (1 min) one. For Hf 2-2, 205 permitted lines are identified in the long-exposure (30 min) spectrum and 202 for the medium-exposure (15 min) spectrum. Table 14 presents the numbers of CELs. In total 50 lines were identified in the long-exposure (20 min) spectrum of NGC 6153 and 35 in the short-exposure (2 min) spectrum, 229 in the long-exposure (30 min) spectrum of M 1-42, 34 for the medium-exposure (15 min) one and 32 for the short-exposure (1 min) spectrum and 32 for the long-exposure (30 min) spectrum of Hf 2-2 and 34 for the medium-exposure (15 min) one.

Nearly 80 O II lines were identified in the deep spectrum of NGC 6153. Additionally, over 70 N II and Ne II lines were identified. Only a handful of C II lines were identified. Similar to the previous analysis of the spectrum of NGC 7009 (Fang & Liu 2011), we noticed that line flux errors generally have a weak dependence on the wavelength, but sensitive to the line strengths. ORLs of C II, N II, O II and Ne II are the most numerous in our spectra, and have typical fluxes of $\sim10^{-4}$–10^{-3} of Hβ, with most of the measurement errors $\sim$10–20 per cent. Errors of the best observed ORLs, such as O II M1 $3p\,^4D^o_{7/2}$ – $3s\,^4P_{5/2}$ λ4649.13, N II M3 $3p\,^3D_3$ – $3s\,^3P^o_2$ λ5679.56, and Ne II M2 $3p\,^4D^o_{7/2}$ – $3s\,^4P_{5/2}$ λ3334.84, have errors much less than 10 per cent. Accurate measurements of these ORLs and others are absolutely essential for conclusive plasma diagnostics and abundance determinations using ORLs.

We have identified more than 200 emission lines in the deep echelle spectra of NGC 6153, M 1-42 and Hf 2-2, with fluxes of the faintest lines measured down to the level $\leqslant10^{-5}$ of the Hβ. Emission lines were identified using the code EMILI. We integrated over the emission line profiles across the whole UVES coverage (3040–10,940 Å) to obtain line fluxes. First, we manually identify all the emission lines in the spectra, utilizing the state-of-the-art atomic database, and constructed a preliminary emission line table that contains the information of wavelengths and fluxes. Later on, all items in the line table were further identified using EMILI, and the results were double-checked. Table 2 is the final line list of the three PNe.

8 SUMMARY AND CONCLUSIONS

We present deep echelle spectra of three Galactic high-ADF PNe NGC 6153, M 1-42 and Hf 2-2. The spectra were obtained with UVES on the ESO 8.2 m VLT. The high-resolution spectra cover a broad wavelength range (∼3040–11 000 Å). Numerous ORLs of the C, N, O and Ne ions were well detected in our spectra. We analyzed the heavy element ORLs using the newly calculated N II and O II effective recombination coefficients. Results of plasma diagnostics and abundance determinations based on ORLs were compared with those derived from CELs.

We present critical analyses of the optical recombination lines of heavy elements observed in the UVES spectra of NGC 6153, M 1-42 and Hf 2-2. In our UVES spectra of the three PNe, we have detected several hundred emission lines, and 74 per cent of them are relatively faint permitted lines. We carefully identified all emission lines using the line-identification code EMILI. Emission line fluxes of the heavy elements, mostly emitted by C II, N II, O II and Ne II, were measured. Tables of line fluxes were compiled so that they can be readily used by the astrophysical communities. The electron temperatures derived from the ratios of the N II and O II ORLs are close to 1000 K, which is lower than the average CEL temperature by one order of magnitude. The N^{2+}/H^{+}, O^{2+}/H^{+} and Ne^{2+}/H^{+} ionic abundance ratios derived from ORLs are higher than their CEL counterparts. ADFs of the heavy elements in this paper are generally consistent with the literature. The deep echelle spectra presented in this paper are not only critical for the basic nebular analysis, but also important for future detailed photoionization modeling of these high-ADF PNe, which will help to reveal the probable origin of the abundance and temperature discrepancies. Although our current treatment of the recombination and collisional-radiative processes of N II (Fang, Storey & Liu 2011, 2013) and O II (P. J. Storey, unpublished; private communications) in gaseous nebulae has been a great improvement over previous work, the atomic data for the Ne II recombination lines that are adequate for the deep spectroscopy of nebulae are still missing. New quantum-mechanical calculations of the Ne II effective recombination coefficients are now in progress.

Through the past decades, innovation of the observational techniques that enables accurate measurements of the faint ORLs of heavy elements and improvement in the calculations of atomic data, especially the recombination theories of the 2nd-row elements (C, N, O, and Ne) in nebular conditions, have help us to better understand the ORL versus CEL "abundance and temperature discrepancies" observed in PNe (also in H II regions). Although several mechanisms have been raised to explain the observed discrepancies in the nebulae, including temperature fluctuations, density inhomogeneities, bi-abundance nebular model, and the κ-distributed electrons, considerable debate of these problems continues. Future high-spatial and high-spectral resolution spectroscopy with the next-generation large telescopes may advance the study of these long-standing problems, and even stimulate new topics in nebular astrophysics. In the meantime, sophisticated photoionization modeling as well as relativistic quantum-mechanical calculations of the atomic data for nebular physics, is still needed to reach further understanding in this area.

ACKNOWLEDGEMENTS

We thank the anonymous referee, whose comments and suggestions have greatly improved this article. Yong Zhang from the University of Hong Kong (HKU) is acknowledged for discussion. We thank Peter J. Storey from University College London (UCL) for providing us the effective recombination coefficients of the O II nebular lines as well as some of the Ne II 4f – 3d transitions before publication. Support from the Natural Science Foundation of China (No. 10933001) is acknowledged.

REFERENCES

Aggarwal K. M., 1983, ApJS, 52, 387
Asplund M., Grevesse N., Jacques Sauval A., Scott, P., 2009, ARA&A, 47, 481
Barker T., 1982, ApJ, 253, 167
Barker T., 1991, ApJ, 371, 217
Bastin R. J., Storey P. J., 2006, IAU Symp., Planetary Nebulae in our Galaxy and Beyond, Proceedings of the International Astronomical Union, Symposium 234. Edited by Michael J. Barlow and Roberto H. Méndez. Cambridge: Cambridge University Press, p.369
Bauman R. P., Porter R. L., Ferland G. J., MacAdam K. B., 2005, ApJ, 628, 541
Benjamin R. A., Skillman E. D., Smits D. P., 1999, ApJ, 514, 307
Benjamin R. A., Skillman E. D., Smits D. P., 2002, ApJ, 569, 288
Berrington K. A., Burke P. G., 1981, P&SS, 29, 377
Blum R., Pradhan A. K., 1992, ApJS, 80, 425
Borkowski K. J., Harrington J. P., Tsvetanov Z., Clegg R. E. S, 1993, ApJL, 415, L47
Borkowski K. J., Harrington J. P., Tsvetanov Z., 1995, ApJL, 449, L143
Brocklehurst M., 1972, MNRAS, 157, 211
Butler K., Zeippen C. J., 1989, A&A, 208, 337
Butler K., Zeippen C. J., 1994, A&AS, 108, 1
Cahn J. H., Kaler J. B., Stanghellini L., 1992, A&AS, 94, 399
Cardelli J. A., Clayton G. C., Mathis J. S., 1989, ApJ, 345, 245
Corradi R. L. M., García-Rojas J., Jones D., Rodríguez-Gil P., 2015, ApJ, 803, 99
D'Odorico S., Cristiani S., Dekker H., Hill V., Kaufer A., Kim T., Primas F., 2000, Proc. SPIE, 4005, 121
Davey A. R., Storey P. J., Kisielius R., 2000, A&A, 142, 85
Dekker H., D'Odorico S., Kaufer A., Delabre B., Kotzlowski H., 2000, Proc. SPIE, 4008, 534
Dopita M. A., Sutherlnd R. S., Nicholls D. C., Kewley L. J., Vogt Frédéric P. A., 2013, ApJS, 208, 10
Ercolano B., Barlow M. J., Storey P. J., Liu X.-W., Rauch T., Werner K., 2003, MNRAS, 344, 1145
Escalante V., Victor G. A., 1990, ApJS, 73, 513
Fang Z., Kwong H. S., Parkinson W. H., 1993, ApJ, 413, L141
Fang X., Liu X.-W., 2011, MNRAS, 415, 181
Fang X., Storey P. J., Liu X.-W., 2011, A&A, 530, A18
Fang X., Liu X.-W., 2013, MNRAS, 40, 1705
Fang X., Storey P. J., Liu X.-W., 2011, A&A, 550, C2
Ferland G. J., 2003, ARA&A, 41, 517
García-Rojas J., Esteban C., 2007, ApJ, 670, 457
Garnett D. R., Dinerstein H. L., 2001, ApJ, 558, 145
Gerhard O., Arnaboldi M., Freeman K. C., Kashikawa N., Okamura S., Yasuda N., 2005, ApJL, 621, L93
Gerhard O., Arnaboldi M., Freeman K. C., Okamura S., Kashikawa N., Yasuda N., 2007, A&A, 468, 815
Grandi S. A., 1976, ApJ, 206, 658
Hamuy M., Walker A. R., Suntzeff N. B., Gigoux P., Heathcote S. R., Phillips M. M., 1992, PASP, 104, 533

Hamuy M., Phillips M. M., Williams R., Krautter J., 1994, PASP, 106, 566
Hirata R., Horaguchi T., 1995, Atomic Spectral Line List. VizieR Online Data Catalog: VI/69. Originally published in: Department of Astronomy, Faculty of Science, Kyoto University, and National Science Museum, 3-23-1 Hyakunin-Cho, Shinjuku-ku, Tokyo
Howarth I. D., Adams, S., 1981, Program EQUIB, Univ. Coll. London, London
Iben I. Jr, Kaler J. B., Truran J. W., Renzini A., 1983, ApJ, 264, 605
Jones D., Wesson R., García-Rojas J., Corradi R. L. M., Boffin H. M. J., 2016, MNRAS, 455, 3263
Keenan F. P., Hibbert A., Ojha P. C., Conlon E. S., 1993, Phys. Scripta., 48, 129
Keenan F. P., Aller L. H., Bell K. L., Hyung S., McKenna F. C., Ramsbottom C. A., 1996, MNRAS, 281, 1073
Kingsburg R. L., Barlow M. J., 2002, A&A, 387, 1135
Kisielius R., Storey P. J., Davey A. R., Neale L. T., 1998, A&AS, 133, 257
Kisielius R., Storey P. J., 2002, A&A, 387, 1135
Kwok S., 2000, The Origin and Evolution of Planetary Nebulae. Cambridge University Press.
Liu X.-W., Danziger I. J., 1993, MNRAS, 263, 256
Liu X.-W., Storey P. J., Barlow M. J., Clegg R. E. S., 1995, MNRAS, 272, 369
Liu X.-W., Storey P. J., Barlow M. J., Danziger I. J., Cohen M., Bryce M., 2000, MNRAS, 312, 585
Liu X.-W., Luo S.-G., Barlow M. J., Danziger I. J., Storey P. J., 2001, MNRAS, 327, 141
Liu X.-W., 2003, in Kwok S., Dopita M., Sutherland R., eds, Proc. IAU Symp. 209, Planetary Nebulae: Their Evolution and Role in the Universe. Astron. Soc. Pac., San Francisco, p. 339
Liu Y., Liu X.-W., Barlow M. J., 2004a, MNRAS, 353, 1251
Liu Y., Liu X.-W., Luo S.-G., Barlow M. J., 2004b MNRAS, 353, 1231
Liu X.-W., Barlow M. J., Zhang Y., Bastin R. J., Storey P. J., 2006, MNRAS, 368, 1959
Liu X.-W., 2006a, in: Walsh J., Stanghellini L., Douglas N., eds., Planetary Nebulae beyond the Milky Way (Berlin: Springer-Verlag), p. 169
Liu X.-W., 2006b, In: Barlow M. J., Méndez R. H. eds., Planetary Nebulae in our Galaxy and Beyond, Proc. IAU Symp. 234 (Cambridge: Cambridge University Press) p. 219
Liu X.-W., 2012a, in York D. G., Gingerich O., Zhang S.-N., Harper C. L., eds, New Vision 400: Engaging Big Questions in Astronomy and Cosmology Four Hundred Years after the Invention of the Telescope. CRC Press, p. 103
Liu X.-W., 2012b, In: Barlow M. J., Méndez R. H. (eds.), Planetary Nebulae: An Eye to the Future, Proc. IAU Symp., Volume 283, p. 131
Longobardi A., Arnaboldi M., Gerhard O., Hanuschik R., 2015a, A&A, 579, A135
Longobardi A., Arnaboldi M., Gerhard O., Mihos J. C., 2015b, A&A, 579, L3
Luo S.-G., Liu X.-W., Barlow M. J., 2001, MNRAS, 326, 1049
Lutz J., et al., 1998, AAS, 192, 894
Menzel D. H., Aller L. H., 1941, ApJ, 94, 30
Mathis J. S., 1957, ApJ, 125, 318
Mendoza C., Zeippen C. J., 1982, MNRAS, 198, 127
Mendoza C., 1983, in IAU Symp. 103, Planetary Nebulae, eds. Flower D. R., Reidel D. (Dordrecht: Kluwer), p. 143
McNabb I. A., Fang X., Liu X.-W., Bastin R. J., Storey P. .J., 2013, MNRAS, 428, 3443
Nicholls D. C., Dopita M. A., Sutherland R. S., 2012, ApJ, 752, 148
Nicholls D. C., Dopita M. A., Sutherland R. S., Kewley L. J., Palay, E., 2013, ApJS, 207, 21
Nussbaumer H., Rusca C., 1979, A&A, 72, 129
Nussbaumer H., Storey P. J., 1981, A&A, 99, 177
Nussbaumer H., Storey P. J., 1984, A&AS, 56, 293
Nussbaumer H., Storey P. J., 1984, A&AS, 69, 123
Osterbrock D. E., Ferland G. J., 2006, Astrophysics of Gaseous Nebulae and Active Galactic Nuclei. University Science Books, Sausalito
Pelan J., Berrington K. A., 1983, ApJ, 270, 758
Péquignot D., Liu X.-W., Barlow M. J., 2003, in Kwok S., Dopita M., Sutherland R., eds, Proc. IAU Symp. 209, Planetary Nebulae: Their Evolution and Role in the Universe. Astron. Soc. Pac., San Francisco, p. 347
Péquignot D., Petitjean P., Boisson C., 1991, A&A, 251, 680
Peimbert M., 1967, ApJ, 150, 825
Peimbert M., 1971, Bol. Obs. Tonantzintla y Tacubaya, 6, 29
Peimbert M., Peimbert A., 2006, In: Barlow M. J., Méndez R. H. eds., Planetary Nebulae in our Galaxy and Beyond, Proc. IAU Symp. 234 (Cambridge: Cambridge University Press) p. 227
Porter R. L., Bauman R. P., Ferland G. J., MacAdam K. B., 2005, ApJL, 622, L73
Porter R. L., Ferland G. J., Storey P. J., Detisch M. J., 2012, MNRAS, 425, L28
Pradhan A. K., 1976, MNRAS, 177, 31
Robertson-Tessi M., Garnett D., 2005, ApJS, 157, 371
Rubin R. H., 1986, ApJ, 309, 334
Rubin R. H., 1989 ApJS, 69, 897
Sawey P. M. J., Berrington K. A., 1993, At. Data Nucl. Data Tables, 55, 81
Sharpee B., Williams R., Baldwin J. A., van Hoof, P. A. M., 2003, ApJS, 149, 157
Sharpee B., Baldwin J. A., Williams R. E., 2004, ApJ, 65, 323
Smits D. P., 1996, MNRAS, 278, 683
Spitzer L. J., 1948, ApJ, 107, 6
Stafford R. P., Bell K. L., Hibbert A., Wijesundera W. P., 1994, MNRAS, 268, 816
Stasińska G., 1978, MNRAS, 66, 257
Storey P. J., 1994, A&A, 282, 999
Storey P. J., Hummer D. G., 1995, MNRAS, 272, 41
Storey P. J., Sochi T., 2013, MNRAS, 430, 598
Storey P. J., Sochi T., 2014, MNRAS, 440, 2581
Storey P. J., Sochi T., 2015a, MNRAS, 446, 1864
Storey P. J., Sochi T., 2015b, MNRAS, 449, 2974
Tsamis Y. G., Barlow M. J., Liu X.-W., Danziger I. J., Storey P. J., 2003, MNRAS, 345, 186
Tsamis Y. G., Barlow M. J., Liu X.-W., et al., 2004, MNRAS, 353, 953
Viegas S. M., Clegg R. E. S., 1994, MNRAS, 271, 993
Vujnovic V., Weise W. L., 1992, J. Phys. Chem. Ref. Data, 21, 919
Wang W., Liu X.-W., 2007, MNRAS, 381, 669
Wesson R., Liu X.-W., Barlow M. J., 2003, MNRAS, 340, 253
Wesson R., Liu X.-W., 2004, MNRAS, 351, 1026
Wesson R., Liu X.-W., Barlow M. J., 2005, MNRAS, 362, 424
Wesson R., Barlow M. J., Liu X.-W., Storey P. J., Ercolano B., De Marco, O., 2008, MNRAS, 383, 1639
Wyse A. B. 1942, ApJ, 95, 356

Yuan H.-B., Liu X.-W., Péquignot D., Rubin R. H., Ercolano B., Zhang Y., 2011, MNRAS, 411, 1035
Zeippen C. J., 1982, MNRAS, 198, 111
Zhang Y., Liu X.-W., Luo S.-G., Péquignot D.,Barlow M. J., 2005a, A&A, 442, 249
Zhang Y., Liu X.-W., Liu Y., Rubin R. H., 2005b, MNRAS, 358, 457
Zhang Y., Liu X.-W., Wesson R., Storey P. J., Liu Y., Danziger I. J., 2004, MNRAS, 351, 935
Zhang Y., Liu X.-W., Zhang B., 2014, ApJ, 780, 93

APPENDIX A: THE SPECTRA

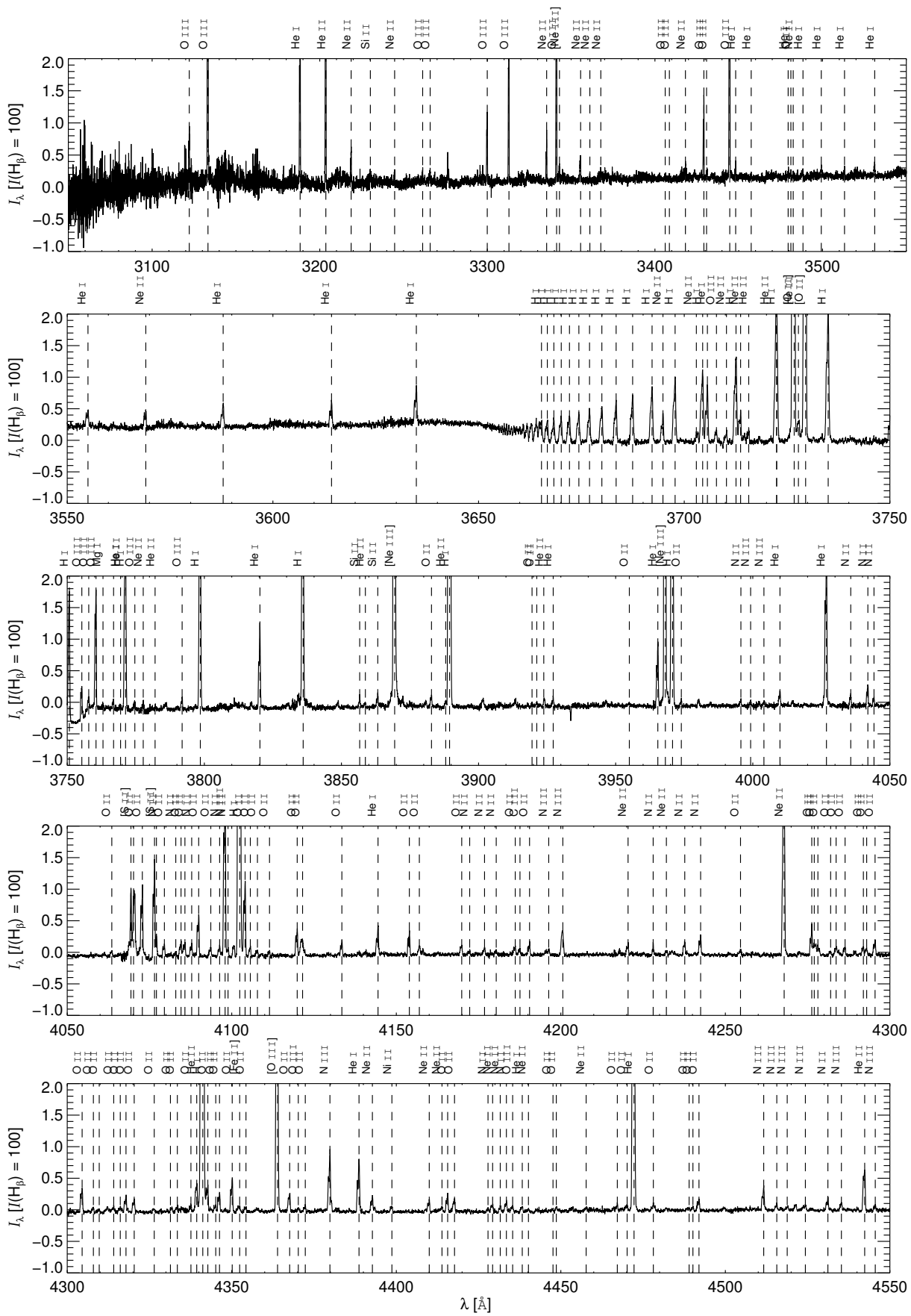

Figure A1. The long-exposure spectra of NGC 6153, M 1-42 and Hf 2-2 from ∼3040 to 10,600 Å. Extinction has not been corrected for. Spectra are normalized such that Hβ has an integrated flux of 100. The spectrum of NGC 6153 is presented here as an example. Readers may contact the corresponding author for the spectra of the other two PNe.

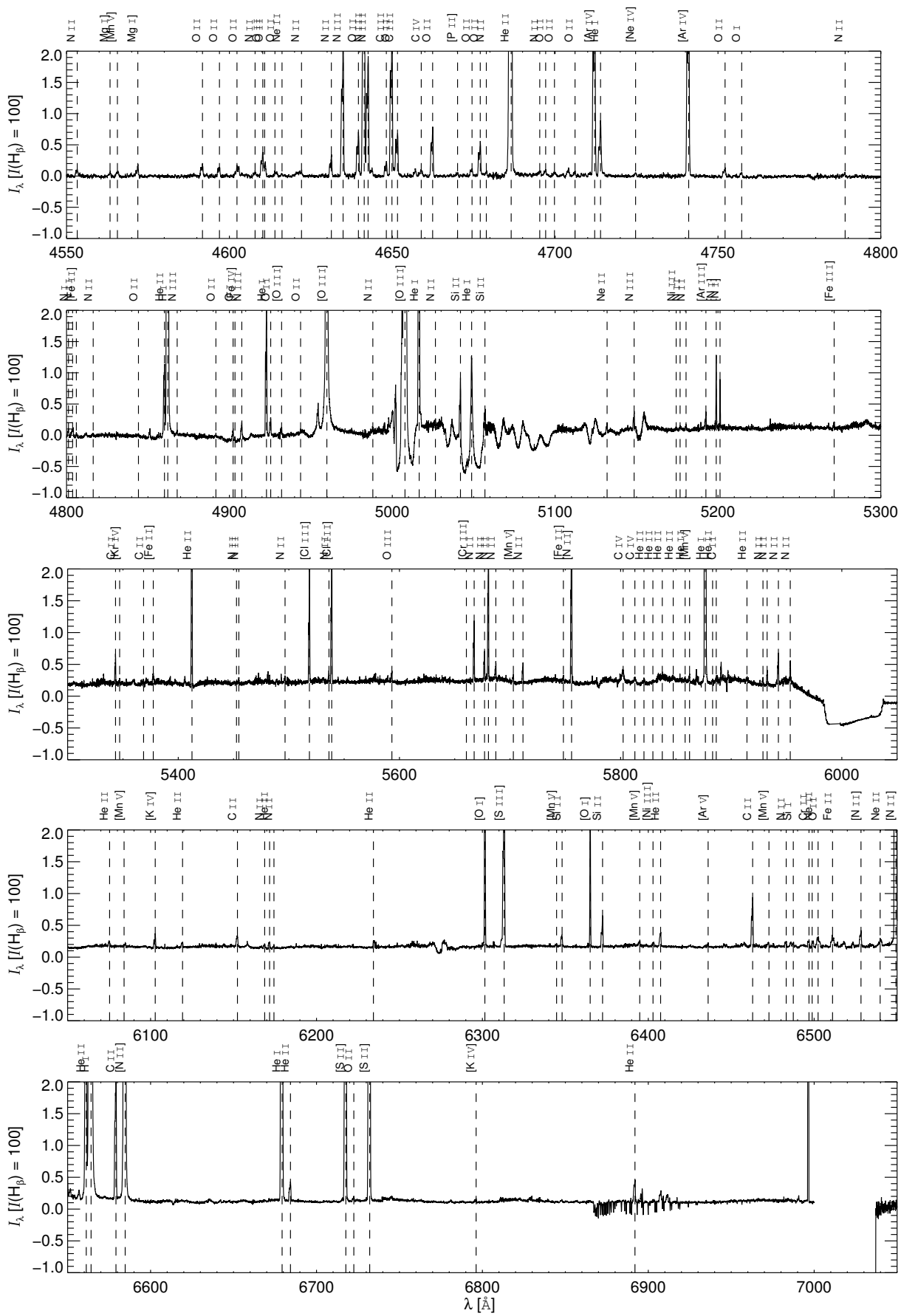

Figure A1. (Continued)

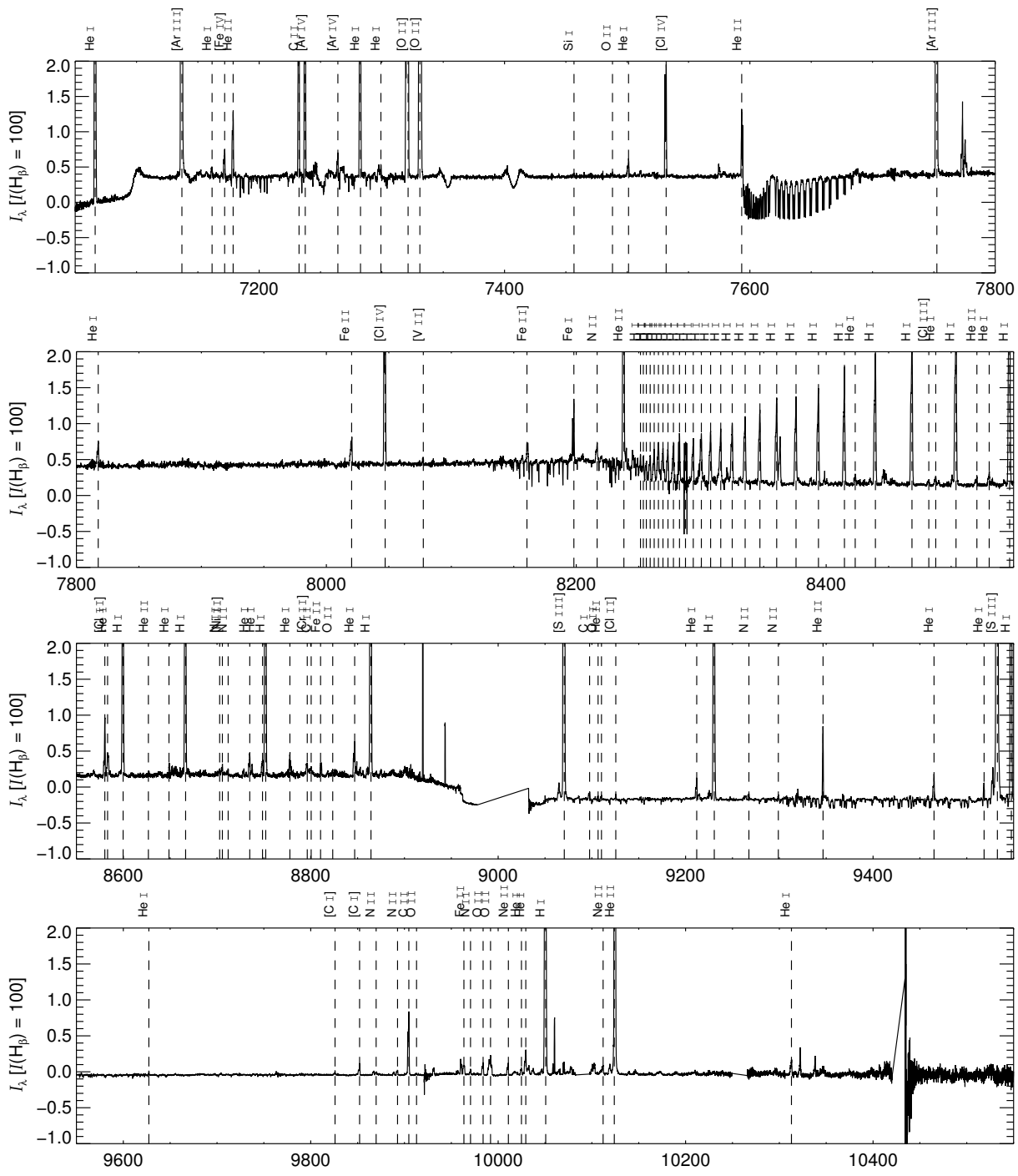

Figure A1. (Continued)